

1 **Dust storms from the Taklamakan Desert significantly darken snow**  
2 **surface on surrounding mountains**

3 Yuxuan Xing<sup>1</sup>, Yang Chen<sup>1</sup>, Shirui Yan<sup>1</sup>, Tenglong Shi<sup>1,2</sup>, Xiaoyi Cao<sup>1</sup>, Xiaoying Niu<sup>1</sup>,  
4 Dongyou Wu<sup>1</sup>, Jiecan Cui<sup>1,3</sup>, Xin Wang<sup>1</sup>, Yue Zhou<sup>1</sup>, Wei Pu<sup>1</sup>

5 <sup>1</sup>Key Laboratory for Semi-Arid Climate Change of the Ministry of Education, College of Atmospheric  
6 Sciences, Lanzhou University, Lanzhou 730000, China

7 <sup>2</sup> Henan Industrial Technology Academy of Spatial-Temporal Big Data, Henan University, Kaifeng  
8 475004, China

9 <sup>3</sup>Zhejiang Development & Planning Institute, Hangzhou 310030, China

10 *Correspondence to:* Wei Pu (puwei@lzu.edu.cn)

11

## 12 **Abstract**

13 The Taklamakan Desert (TD) is a major source of mineral dust emissions into the  
14 atmosphere. These dust particles have the ability to darken the surface of snow on the  
15 surrounding high mountains after deposition, significantly impacting the regional  
16 radiation balance. However, previous field measurements have been unable to capture  
17 the effects of severe dust storms accurately, and their representation on regional scales  
18 has been inadequate. In this study, we propose a modified remote-sensing approach that  
19 combines data from the Moderate Resolution Imaging Spectroradiometer (MODIS)  
20 satellite and simulations from the Snow, Ice, and Aerosol Radiative (SNICAR) model.  
21 This approach allows us to detect and analyze the substantial snow darkening resulting  
22 from dust storm deposition. We focus on three typical dust events originating from the  
23 Taklamakan Desert and observe significant snow darkening over an area of  $\sim 2160$ ,  
24  $\sim 610$ , and  $\sim 640$  km<sup>2</sup> in the Tien Shan, Kunlun, and Qilian Mountains, respectively. Our  
25 findings reveal that the impact of dust storms extends beyond the local high mountains,  
26 reaching mountains located approximately 1000 km away from the source. Furthermore,  
27 we observe that dust storms not only darken the snowpack during the spring but also in  
28 the summer and autumn seasons, leading to increased absorption of solar radiation.  
29 Specifically, the snow albedo reduction (radiative forcing) triggered by severe dust  
30 depositions is up to 0.028–0.079 (11–31.5 W m<sup>-2</sup>), 0.088–0.136 (31–49 W m<sup>-2</sup>), and  
31 0.092–0.153 (22–38 W m<sup>-2</sup>) across the Tien Shan, Kunlun, and Qilian Mountains,  
32 respectively. This further contributes to the aging of the snow, as evidenced by the  
33 growth of snow grain size. Comparatively, the impact of persistent but relatively slow  
34 dust deposition over several months during non-event periods is significantly lower  
35 than that of individual dust event. This highlights the necessity of giving more attention  
36 to the influence of extreme events on the regional radiation balance. From this study,  
37 we gain a deeper understanding of how a single dust event can affect the extensive  
38 snowpack and demonstrates the potential of employing satellite remote-sensing to  
39 monitor large-scale snow darkening.

## 40 **1 Introduction**

41 High Mountain Asia (HMA), which includes the Tibetan Plateau (TP) and surrounding  
42 mountain ranges, holds the largest amount of glaciers and snow outside of the poles.  
43 This region is informally known as the “The Third Pole” and the “Asian Water Tower”  
44 (Yao et al., 2012, 2019) because of its extreme importance as a freshwater source, with  
45 approximately one billion people relying on the water and hydropower that the glaciers  
46 and snow across HMA regularly provide (Immerzeel et al., 2012; Mishra et al., 2018).  
47 The snow-covered area of HMA is a highly reflective natural surface that has a  
48 significant impact on the regional radiation balance (Cohen and Rind, 1991; Painter et  
49 al., 2012). Previous satellite and ground-based observations have demonstrated that the  
50 mass and extent of the snow cover across HMA are rapidly declining owing to recent  
51 global warming (Bormann et al., 2018; Notarnicola et al., 2020; Pulliainen et al., 2020).  
52 Furthermore, growing evidence has indicated that light-absorbing particles (LAPs)  
53 (Arun et al., 2019, 2021a, 2021b; Chaubey et al., 2010; Gogoi et al., 2018, 2021a; 2021b;  
54 Thakur et al., 2021), such as mineral dust and black carbon (BC), can induce snow  
55 darkening effect when they are deposited on the snow surface (Wang et al., 2013; Qian  
56 et al., 2015; Dang et al., 2017; Huang et al., 2022; Niu et al., 2022; Réveillet et al.,  
57 2022). This snow darkening effect increases solar absorption and decreases snow  
58 albedo, resulting in enhanced snowmelt (Hadley and Kirchstetter, 2012; Dumont et al.,  
59 2014; He et al., 2017, 2018; Shi et al., 2021, 2022a, 2022b; Cordero et al., 2022) and  
60 an accelerated transformation of ice and snow into liquid water in the Asian Water  
61 Tower (Yao et al., 2022). Consequently, the snow-darkening effect plays a critical role  
62 in snow decline across HMA, thereby perturbing the climate system and impacting  
63 hydrological cycles (Kraaijenbrink et al., 2017, 2021; Sang et al., 2019; Shi et al., 2019;  
64 Zhang et al., 2020, 2021; Roychoudhury et al., 2022; Yang et al., 2022).

65 The Taklamakan Desert (TD) in southwestern Xinjiang, Northwest China, is the  
66 second-largest shifting sand desert on Earth and accounts for 42% of all dust emissions  
67 in East Asia (Chen et al., 2017a). Approximately 70.54 Tg of dust are emitted into the  
68 atmosphere annually, with the most intense dust events occurring in spring (Chen et al.,  
69 2017a). The dust in the Tarim Basin is predominantly redeposited onto nearby regions  
70 owing to the surrounding high mountains (Qiu et al., 2001; Sun et al., 2001; Shao and

71 Dong, 2006). When the dust is uplifted above 4 km altitude, it may eventually settle on  
72 the snow surfaces across the surrounding high mountains, such as the Tien Shan and  
73 Kunlun Mountains and subsequently induce a snow-darkening effect (Ge et al., 2014;  
74 Jia et al., 2015; Yuan et al., 2018). Furthermore, this dust is also transported eastward  
75 beyond the Tarim Basin and can be transported all the way to the Qilian Mountains via  
76 the westerly winds during spring and summer, thereby inducing a snow darkening effect  
77 in this distal region to the east of the TD (Dong et al., 2020; Han et al., 2022). Therefore,  
78 TD dust may have a profound effect on the regional radiative balance by darkening the  
79 snow across the high mountains surrounding the TD. This effect may subsequently  
80 accelerate snow melting and affect water resources for the 30+ million people living in  
81 the Xinjiang and Gansu provinces of China (Mishra et al., 2021).

82 Numerous field measurements have been undertaken in recent decades to investigate  
83 the dust content of snow/glaciers across the high mountains surrounding the TD, with  
84 measured dust contents generally varying from 1.4 to 110  $\mu\text{g g}^{-1}$  (Wake et al., 1994;  
85 Dong et al., 2009, 2014; Wu et al., 2010; Ming et al., 2016; Xu et al., 2016; Schmale et  
86 al., 2017; Zhang et al., 2018, 2021; Wang et al., 2019; Li et al., 2021, 2022). This  
87 abundance of dust particles has been found to induce a significant snow darkening  
88 effect across the high-mountain snowpack, thereby increasing its associated radiative  
89 forcing to 25.8–65.7  $\text{W m}^{-2}$ . Furthermore, the estimated natural dust-induced snow-  
90 darkening effect can be equivalent to that induced by BC, particularly during intense  
91 springtime dust events\_(Sarangi et al., 2020; Zhang et al., 2021). These findings  
92 effectively highlight the significance of the TD dust-induced snow darkening effect  
93 across the surrounding high mountains. In spite of these invaluable in situ findings,  
94 ground-based observations are poorly represented at the regional scale owing to limited  
95 spatial coverage and temporal discontinuity (Arun et al., 2019). Furthermore, these  
96 previous field measurements may not be able to capture severe dust emission and  
97 loading events, which are more likely to induce snow darkening than common dry and  
98 wet deposition processes (Dumont et al., 2020; Pu et al., 2021; Baladima et al., 2022).

99 Satellite remote sensing offers an effective way to overcome the limitations of ground-

100 based measurements by providing a more comprehensive understanding of the LAP-  
101 induced impact on the regional radiative forcing of the snowpack (Skiles et al., 2018a).  
102 For example, Painter et al. (2012) found that the instantaneous LAP-induced radiative  
103 forcing can exceed  $250 \text{ W m}^{-2}$  in the Hindu Kush-Himalaya region via an analysis of  
104 Moderate Resolution Imaging Spectroradiometer (MODIS) satellite data. Sarangi et al.  
105 (2020) further revealed that dust is the primary factor responsible for high-altitude snow  
106 darkening in the Hindu Kush–Himalaya region. Similarly, severe dust events from the  
107 Sahara can deposit dust on the snowpack across the European Alps and Caucasus  
108 Mountains (Di Mauro et al., 2015; Dumont et al., 2020), with this deposition inducing  
109 a radiative forcing of up to  $153 \text{ W m}^{-2}$  based on satellite retrievals in Europe. Dust  
110 deposition has also induced extensive snow darkening across the Upper Colorado River  
111 Basin in North America, particularly during extreme dust events (Skiles et al., 2016,  
112 2018b; Painter et al., 2017). These studies have demonstrated the effectiveness of  
113 employing satellite remote sensing to estimate the dust content of the snowpack and its  
114 associated radiative forcing. However, detecting natural dust deposition on the snow  
115 surfaces across high mountains surrounding the TD is still limited.  
116 Here we investigate the impact of dust storms on snow albedo reduction and radiative  
117 forcing across the high mountains surrounding the TD. We first capture three typical  
118 dust events that induced snow darkening in the Tien Shan, Kunlun, and Qilian  
119 Mountains, respectively. We then utilize MODIS satellite data and the Snow, Ice, and  
120 Aerosol Radiative (SNICAR) model to retrieve the dust content of the snowpack. We  
121 then capture three typical dust events that induced snow darkening in the Tien Shan,  
122 Kunlun, and Qilian Mountains, respectively. Finally, we analyze the spatial and  
123 altitudinal variations in dust-induced snow darkening and compare our retrievals with  
124 field measurements. Through remote sensing observations, we aim to provide a new  
125 view of the darkening effect of natural desert dust on the snowpack of the high  
126 mountains surrounding the TD.

## 127 **2 Methodology**

### 128 **2.1 Remote-sensing data**

129 We accessed two MODIS datasets, the surface reflectance (MOD09GA:  
130 <https://earthdata.nasa.gov>; 500 × 500 m resolution) and aerosol optical depth (AOD;  
131 MCD19A2), to evaluate the impact of dust on snow albedo. MOD09GA is the daily  
132 surface reflectance product after the atmospheric correction from the Terra satellite,  
133 which provides the reflectance data for seven bands (band 1, 620–670 nm; band 2, 841–  
134 876 nm; band 3, 459–479 nm; band 4, 545–565 nm; band 5, 1230–1250 nm; band 6,  
135 1628–1652 nm; band 7, 2105–2155 nm). Previous studies have indicated that the  
136 MODIS sensor on Terra is not affected by saturation on bright snow surfaces. As a result,  
137 it has the capability of detecting changes in reflectance in the visible (VIS) bands caused  
138 by dust in snow (Painter et al., 2012; Pu et al., 2019). Additionally, we used the updated  
139 MODIS Aerosol Optical Depth (AOD) product MCD19A2, based on the MAIAC  
140 algorithm, to assess the AOD levels during dust events. This is a combined product of  
141 Terra/Aqua with a spatial-temporal resolution of 1km, which were resampled to 500m  
142 resolution using GEE (<https://earthengine.google.com>).

143 The daily averaged downward shortwave flux was obtained from the NASA Clouds  
144 and the Earth's Radiant Energy System (CERES: <https://ceres.larc.nasa.gov>; 1° × 1°  
145 resolution). The CERES data products take advantage of the synergy between  
146 collocated CERES instruments and spectral imagers, such as MODIS (Terra and Aqua)  
147 and the Visual Infrared Imaging Radiometer Suite (S-NPP and NOAA-20). We used the  
148 downward shortwave flux to estimate the daily averaged radiative forcing that was due  
149 to dust deposition on the snowpack. The Cloud-Aerosol Lidar with Orthogonal  
150 Polarization (CALIOP/CALIPSO) provided by NASA is able to detect the type and  
151 height of aerosols in the atmosphere (Huang et al., 2007; Han et al., 2022) and can  
152 therefore be used to identify the movement of dust storms over the high mountains  
153 surrounding the TD.

154 The Shuttle Radar Topography Mission (SRTM) digital elevation data, which possess  
155 a 90-m spatial resolution, were provided by NASA and downloaded from Google Earth  
156 Engine (<https://earthengine.google.com>). These data were used to correct the influence  
157 of topography on surface reflectance.

## 158 **2.2 Snow depth and wind data**

159 The snow depth data were provided by NASA and accessed from the Modern-Era  
160 Retrospective Analysis for Research and Applications, Version 2 (MERRA-2:  
161 <https://gmao.gsfc.nasa.gov>). The MERRA-2 snow depth product was selected because  
162 it has better accuracy than those from ERA-Interim, JJA-55, and ERA5 across HMA  
163 (Orsolini et al, 2019). The wind field data were obtained from the European Centre for  
164 Medium-Range Weather Forecasts (ECMWF) Reanalysis v5 (ERA5:  
165 <https://www.ecmwf.int>) owing to its superior performance in terms of its high spatial  
166 resolution and longer time span compared with other products (Copernicus Climate  
167 Change Service, 2017). Here, we used ERA5 wind data at 700 hPa to describe the  
168 atmospheric circulation during the analyzed dust storms.

### 169 **2.3 Radiative-transfer model**

170 The SNICAR model is a two-stream radiative transfer model (Flanner et al., 2007, 2009)  
171 that has been widely used to simulate the spectral albedo of LAP-contaminated snow  
172 (Sarangi et al., 2019; Chen et al., 2021). The model includes snow properties such as  
173 snow depth and effective radius and accounts for the incident radiation at the surface  
174 and its spectral distribution, solar zenith angle, and the type and concentration of LAPs  
175 in the snowpack. In this study, dust optical parameters are taken from SNICAR defaults,  
176 where the refractive index is  $1.56 + 0.0038i$  at  $0.63 \mu\text{m}$  (Patterson et al., 1981; Flanner  
177 et al., 2007). And a diameter bin of  $0.1\text{-}1 \mu\text{m}$  was selected according to the previous  
178 observations from Taklamakan Desert (Okada and Kai, 2004). Furthermore, a single-  
179 layer snowpack model was adopted in our study, in line with Cui et al. (2021), since the  
180 snow darkening effect typically pertains to surface snow. This simplification minimally  
181 affects the retrieval of LAPs from the surface snow, despite the complex multilayer  
182 structure of natural snowpacks.

183 The Santa Barbara DISORT Atmospheric Radiative Transfer (SBDART) model is one  
184 of the most widely used models for simulating the surface solar irradiance in clear and  
185 cloudy sky conditions (Ricchiazzi et al., 1998). The SBDART model includes standard  
186 atmospheric models, cloud models, extraterrestrial source spectra, gas absorption  
187 models, standard aerosol models, and surface models. Here, we used the SBDART  
188 model to calculate the spectral surface solar irradiance, following the approach of Cui

189 et al. (2021). In this study, the cloud-free condition was set in SBDART, according to  
190 the MODIS images.

#### 191 **2.4 Terrain correction**

192 The high mountains surrounding the TD have a complex terrain, such that the local  
193 solar zenith angle ( $\beta$ ) may differ from the MODIS-derived solar zenith angle ( $\theta_0$ ).  
194 Therefore, the topographic correction method should be used to derive  $\beta$  (Teillet et al.,  
195 1982; Negi and Kokhanovsky, 2011):

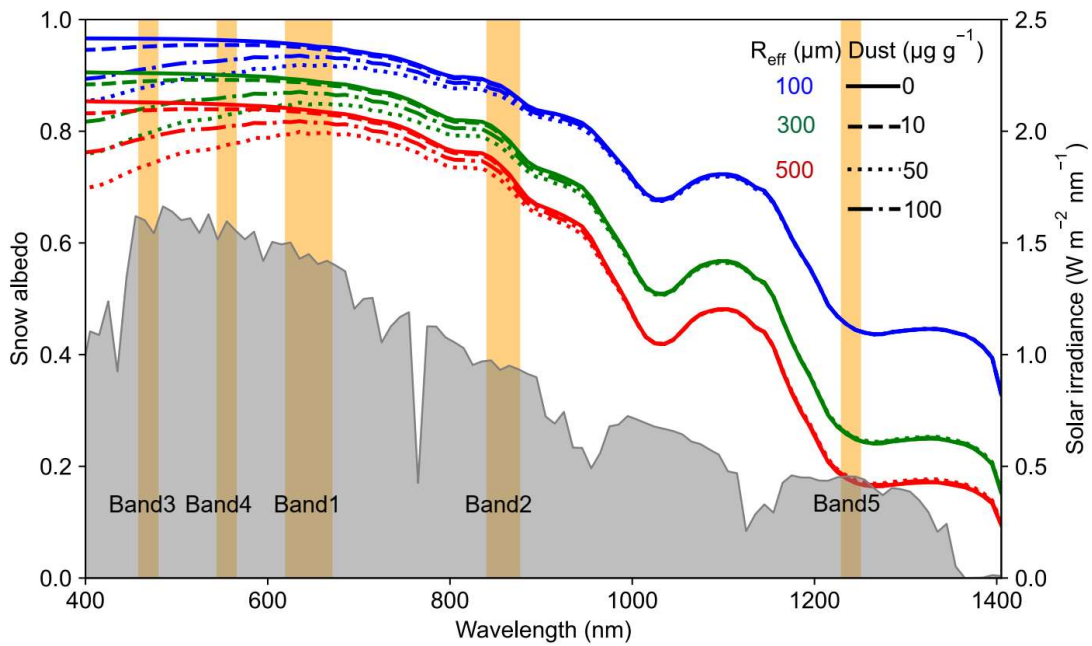
$$196 \cos \beta = \cos \theta_0 \cos \theta_T + \sin \theta_0 \sin \theta_T \cos (\phi_0 - \phi_T), \quad (1)$$

197 where  $\phi_0$  is the solar azimuth angle from MODIS, and  $\theta_T$  and  $\phi_T$  are the surface  
198 slope and aspect from SRTM, respectively. We then replace  $\theta_0$  with  $\beta$  in subsequent  
199 satellite retrievals.

#### 200 **2.5 Snow properties retrieval**

201 The dust-contaminated spectral snow albedo is determined based on the dust content,  
202 snow grain size, snow depth, and solar zenith angle (Wiscombe and Warren, 1980). The  
203 dust content and snow depth primarily impact the snow albedo in the ultraviolet (UV)  
204 and VIS wavelengths, with a much smaller effect on snow albedo in the near infrared  
205 (NIR) wavelengths (Figure 1 and Figure S1). Conversely, the snow grain size and solar  
206 zenith angle primarily impact the snow albedo in the NIR wavelengths. The solar zenith  
207 angle and snow depth data are from MODIS Terra and MERRA-2, respectively. We  
208 used the SNICAR model to derive the quantitative snow grain size and dust content  
209 from the MODIS data. Then the SBDART model was combined to estimate the dust-  
210 induced snow albedo reduction and radiative forcing. Figure 2 shows the flowchart of  
211 the overall retrieval process.





212

213 **Figure 1. Snow albedo spectra for different snow optical effective radius ( $R_{\text{eff}}$ ) and**  
 214 **dust contents that were simulated using the SNICAR model. Orange bars denote**  
 215 **MODIS bands, and the gray region represents the typical solar irradiance in HMA.**

216 The Snow-Covered Area and Grain size (SCAG) model is a spectral unmixing method  
 217 that is widely used for identifying snow cover fraction (SCF) and snow optical effective  
 218 radius ( $R_{\text{eff}}$ ), especially in complex mountain terrains (Painter et al., 2009, 2012; Rittger  
 219 et al., 2013). The SCAG model retrieves the SCF and  $R_{\text{eff}}$  using all seven bands of the  
 220 MODIS reflectance data, which span the VIS to NIR range. It does not consider the  
 221 impact of LAPs. However, in our study, the dust content in snow is extreme high, which  
 222 will significantly reduce the VIS snow albedo in MODIS bands 1, 3, 4 (Figure 1). So,  
 223 the SCAG model will introduce a large bias in the resultant SCF and  $R_{\text{eff}}$  retrievals.  
 224 Furthermore, the reflectance of fine-grained dirty snow has been compared with that of  
 225 pure coarse-grained snow at short-wave infrared wavelengths, which include bands 6  
 226 and 7 (Bair et al., 2020). The extremely high dust content in this study therefore means  
 227 that the reflectance in MODIS bands 6 and 7 is not appropriate for snow property  
 228 retrieval. Instead, we used the reflectance data in MODIS bands 2 and 5 to unmix the  
 229 surface reflectance to derive SCF and  $R_{\text{eff}}$  (Figure 2), similar to the approach in Painter  
 230 et al. (2009). The surface reflectance at band  $i$  ( $R_{\text{band } i}^{\text{MODIS}}$ ) can be expressed as follows

231 (Cui et al., 2021):

$$\begin{aligned}
 232 \quad R_{\text{band } i}^{\text{MODIS}} &= \frac{E_{\text{band } i} \times \text{SCF} \times R_{\text{band } i}^{\text{MODIS, snow}} + E_{\text{band } i} \times (1 - \text{SCF}) \times R_{\text{band } i}^{\text{soil}}}{E_{\text{band } i}} \\
 233 \quad &= \text{SCF} \times R_{\text{band } i}^{\text{MODIS, snow}} + (1 - \text{SCF}) \times R_{\text{band } i}^{\text{soil}}, \quad (2)
 \end{aligned}$$

234 where  $R_{\text{band } i}^{\text{MODIS, snow}}$  and  $R_{\text{band } i}^{\text{soil}}$  represent the snow and soil reflectances at band  $i$ ,  
 235 respectively, with  $R_{\text{band } i}^{\text{soil}}$  taken from Siegmund and Menz (2005), and  $E_{\text{band } i}$  is the  
 236 solar irradiance at band  $i$ . The snow reflectance at band  $i$  ( $R_{\text{band } i}^{\text{MODIS, snow}}$ ) can be  
 237 expressed as

$$238 \quad R_{\text{band } i}^{\text{MODIS, snow}} = \left( \frac{R_{\text{band } i}^{\text{MODIS}} - (1 - \text{SCF}) \times R_{\text{band } i}^{\text{soil}}}{\text{SCF}} \right). \quad (3)$$

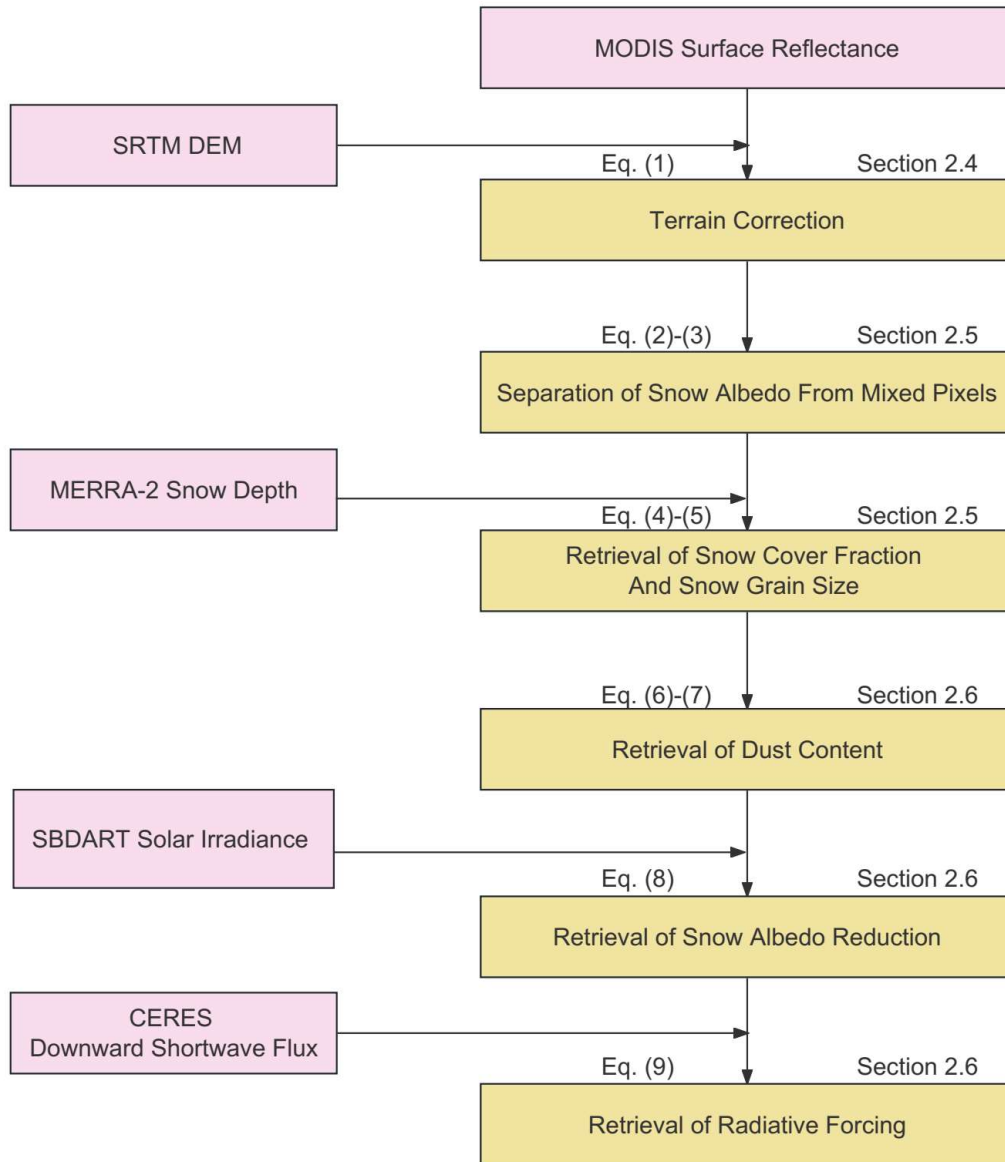
239 We then fit the SNICAR-simulated snow reflectance to the MODIS-derived snow  
 240 reflectance, which is expressed as either

$$241 \quad \text{RMSE} = \left( \frac{1}{2} (a \times (R_{\text{band } 2}^{\text{SNICAR, snow}} - R_{\text{band } 2}^{\text{MODIS, snow}})^2 + (R_{\text{band } 5}^{\text{SNICAR, snow}} - R_{\text{band } 5}^{\text{MODIS, snow}})^2) \right)^{\frac{1}{2}} \quad (4)$$

242 or

$$\begin{aligned}
 243 \quad \text{RMSE} &= \frac{1}{2} (a \times (R_{\text{band } 2}^{\text{SNICAR, snow}} - \left( \frac{R_{\text{band } 2}^{\text{MODIS}} - (1 - \text{SCF}) \times R_{\text{band } 2}^{\text{soil}}}{\text{SCF}} \right))^2 \\
 244 \quad &+ (R_{\text{band } 5}^{\text{SNICAR, snow}} - \left( \frac{R_{\text{band } 5}^{\text{MODIS}} - (1 - \text{SCF}) \times R_{\text{band } 5}^{\text{soil}}}{\text{SCF}} \right))^2) \right)^{\frac{1}{2}}, \quad (5)
 \end{aligned}$$

245 where RMSE is the root mean square error,  $R_{\text{band } i}^{\text{SNICAR, snow}}$  is the SNICAR-simulated  
 246 snow reflectance at band  $i$  (which is dependent on the  $R_{\text{eff}}$  and solar zenith angle, where  
 247 the solar zenith angle is derived from the MODIS data), and  $a$  is an empirical coefficient  
 248 (0.1–1 range). In this study,  $a$  was set to 0.1 to reduce the interference of dust on the  
 249 snow properties retrieval because a high dust content can influence the snow albedo at  
 250 band 2 (Figure 1). We can then derive SCF and  $R_{\text{eff}}$  by minimizing the RMSE (Painter  
 251 et al., 2009).



252

253 **Figure 2. Flowchart illustrating the step-by-step retrieval of dust content and the**  
 254 **associated snow albedo reduction and radiative forcing: the pink boxes denote the**  
 255 **external input data, while the yellow boxes are used for calculations in this study.**

## 256 **2.6 Dust content and snow albedo reduction retrieval**

257 We fit the SNICAR-simulated snow reflectance to the MODIS-derived snow  
 258 reflectance in bands 3 and 4, which are the most sensitive to the dust content in snow,  
 259 following Pu et al. (2019) and Cui et al. (2021), which are expressed as either

$$260 \quad \text{RMSE} = \frac{1}{2} \left( (R_{\text{band 3}}^{\text{SNICAR, snow}} - R_{\text{band 3}}^{\text{MODIS, snow}})^2 + (R_{\text{band 4}}^{\text{SNICAR, snow}} - R_{\text{band 4}}^{\text{MODIS, snow}})^2 \right)^{\frac{1}{2}} \quad (6)$$

261 or

$$\begin{aligned} 262 \text{ RMSE} = & \left( \frac{1}{2} \left( R_{\text{band } 3}^{\text{SNICAR, snow}} - \left( \frac{R_{\text{band } 3}^{\text{MODIS}} - (1 - \text{SCF}) \times R_{\text{band } 3}^{\text{soil}}}{\text{SCF}} \right) \right) \right)^2 \\ 263 & + \left( R_{\text{band } 4}^{\text{SNICAR, snow}} - \left( \frac{R_{\text{band } 4}^{\text{MODIS}} - (1 - \text{SCF}) \times R_{\text{band } 4}^{\text{soil}}}{\text{SCF}} \right) \right)^2 \end{aligned} \quad (7)$$

264 where  $R_{\text{band } 3}^{\text{SNICAR, snow}}$  is a function of four factors: dust content,  $R_{\text{eff}}$ , snow depth, and  
265 solar zenith angle. The latter three factors have been derived, leaving the dust content  
266 as the only unknown. Therefore, the dust content can be retrieved by minimizing Eq.  
267 (7). We assume that the derived dust content in this study accounts for the total light  
268 absorption by all of the LAPs that are present in the snowpack. This is because our  
269 study area is close to the Taklamakan Desert (TD), where large amounts of dust  
270 accumulate on the snow surface annually. In contrast, anthropogenic activities and  
271 biomass burning are rare, resulting in limited depositions of black carbon (BC) and  
272 organic carbon (OC) (Fig. S8). Observations from snow and atmosphere have  
273 confirmed this phenomenon (Wake et al., 1994; Huang et al., 2007). Therefore, our  
274 assumption is plausible.

275 The dust-induced broadband albedo reduction ( $\Delta\alpha$ ) can then be calculated as follows:

$$276 \Delta\alpha = \frac{\sum_{\lambda=300\text{nm}}^{\lambda=2500\text{nm}} E_{\lambda} \cdot (R_{\lambda}^{\text{SNICAR, pure-snow}} - R_{\lambda}^{\text{SNICAR, snow}}) \cdot \Delta\lambda}{\sum_{\lambda=300\text{nm}}^{\lambda=2500\text{nm}} E_{\lambda} \cdot \Delta\lambda}, \quad (8)$$

277 Where  $R_{\lambda}^{\text{SNICAR, pure-snow}}$  and  $R_{\lambda}^{\text{SNICAR, snow}}$  are the SNICAR-simulated pure and  
278 polluted snow albedo using snow grain size and dust content retrieved above, solar  
279 zenith angle from MODIS and snow depth from MERRA2, respectively.  $E_{\lambda}$  represents  
280 the spectral solar irradiance at wavelength  $\lambda$  simulated from the SBDART model,  $\Delta\lambda$  is  
281 10 nm, and  $R_{\lambda}^{\text{SNICAR, pure-snow}}$  and  $R_{\lambda}^{\text{SNICAR, snow}}$  are the SNICAR-simulated pure and  
282 polluted snow albedo, respectively. The spectral irradiance from SBDART is only used  
283 for integrating the spectral MODIS albedo to achieve broadband albedo. Thus, the  
284 uncertainty in solar irradiance from the assumed atmospheric properties has limited  
285 influence on the retrieval of snow albedo reduction (Cui et al., 2021).

286 The dust-induced radiative forcing (RF) is calculated as follows:

287  $RF = \Delta\alpha \cdot SW,$  (9)

288 where SW is the downward shortwave flux, which is obtained from CERES.

289 The in situ dust content was not measured to verify the MODIS retrievals because of  
290 the challenging geographical conditions surrounding the TD. Nevertheless, Cui et al.  
291 (2021) verified a similar retrieval method across the Northern Hemisphere. They  
292 considered that the accuracy of MODIS surface reflectance is typically  $\pm (0.005 + 0.05$   
293  $\times \text{reflectance})$  under conditions where aerosol optical depth (AOD) is less than 5.0, and  
294 solar zenith angle is less than  $75^\circ$ , as stated in the MODIS Surface Reflectance user's  
295 guide (Collection 6; <https://modis.gsfc.nasa.gov/data/dataproduct/mod09.php>, last access:  
296 19 January, 2024). In addition, the bias for snow grain size retrieval was assumed to be  
297 30 % according to the studies of Pu et al. (2019) and Wang et al. (2017). These biases  
298 led to an overall uncertainty ranging from 10% to 110% in the retrieval of LAPs across  
299 the Northern Hemisphere. The study revealed that uncertainty decreased as LAPs  
300 concentration increased, with reported uncertainties dropping to below approximately  
301 30% in regions of high pollution, such as Northeast China. In our study, the snowpack  
302 was also significantly polluted due to severe dust depositions, leading us to consider a  
303 retrieval uncertainty of 30% for LAPs, in alignment with the findings of Cui et al.  
304 (2021). Then, the overall lower bound and upper bound of the uncertainty value of snow  
305 albedo reduction retrieval was calculated and will be discussed in the following section.  
306 Moreover, we utilized the LAPs and the corresponding albedo reduction retrieved at  
307 the local time of 10:30 AM (the time of the MODIS Terra satellite overpass), as the  
308 proxy for daily averages following Painter et al. (2012). This approximation was  
309 reasonable, given that the content of LAPs exhibited little variation over a diurnal cycle  
310 (Painter et al., 2009; Zege et al., 2011). The variation in snow albedo throughout the  
311 day was primarily attributed to changes in the solar zenith angle (Figure S1). Since the  
312 solar zenith angle predominantly influences snow albedo in NIR, with little impact on  
313 the VIS, the diurnal variation in LAPs-induced snow albedo reduction was also  
314 considered limited.

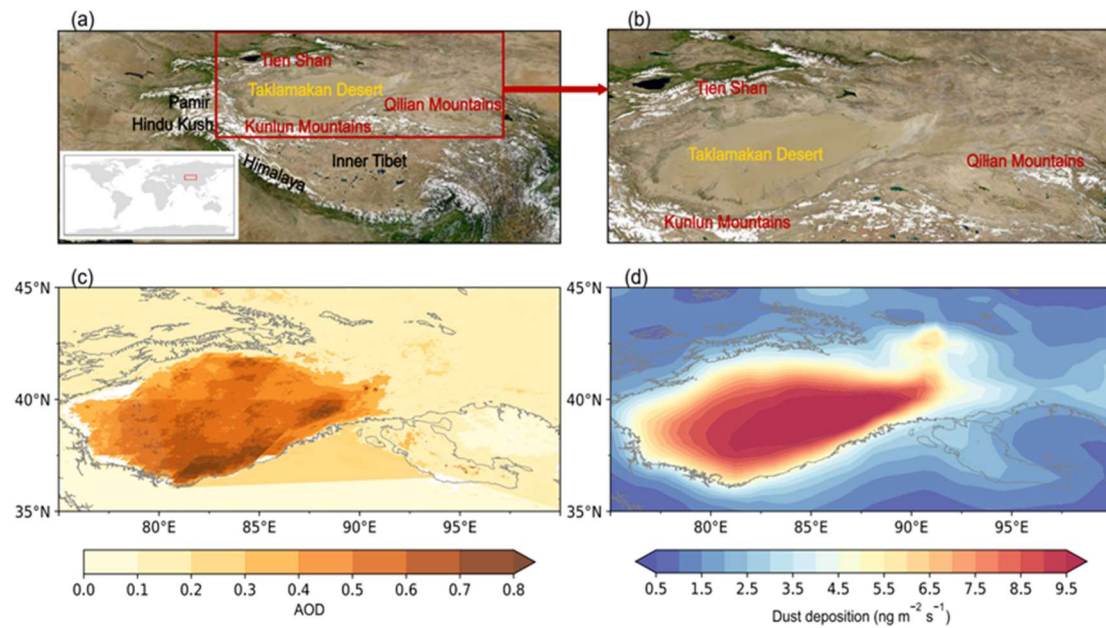
315 As noted above, the snow albedo reduction is mainly dependent on the dust content,  
316  $R_{\text{eff}}$ , snow depth, and solar zenith angle. The  $R_{\text{eff}}$  and snow depth can be categorized as

317 snow properties. We compared the dust content, snow properties, and solar zenith angle  
318 to discuss their contributions to the spatial variations in snow albedo reduction (Pu et  
319 al, 2019; Cui et al., 2021). The supplementary information contains a thorough  
320 derivation of this method.

### 321 **3 Results**

#### 322 **3.1 Remote sensing of the snow darkening effect across the high mountains** 323 **surrounding the TD**

324 The TD is located in the northern part of HMA and is surrounded by some of the highest  
325 mountain ranges on Earth, including the Kunlun Mountains, Tien Shan, and Pamir  
326 (Figures 3a and b). The TD region emits vast amounts of dust particles into the  
327 atmosphere each year, particularly during the spring and summer (Wang et al., 2008;  
328 Chen et al., 2013, 2017b; Kang et al., 2016; Wu et al., 2021; Tang et al., 2022); this  
329 phenomenon is confirmed by the high AOD levels at 550 nm from March to August  
330 (Figure 3c). A significant amount of this dust is ultimately redeposited across the Tarim  
331 Basin and the surrounding mountains. The Tien Shan and Kunlun Mountains are two  
332 regions that experience high levels of dust deposition owing to the local topography  
333 and atmospheric circulation patterns (Figure 3d) (Huang et al., 2007, 2014; Ge et al.,  
334 2014; Dong et al., 2022). Therefore, we selected two typical cases to demonstrate the  
335 snow-darkening effect across the mountains surrounding the TD, a springtime dust  
336 event across the Tien Shan and a summertime dust event across the Kunlun Mountains.



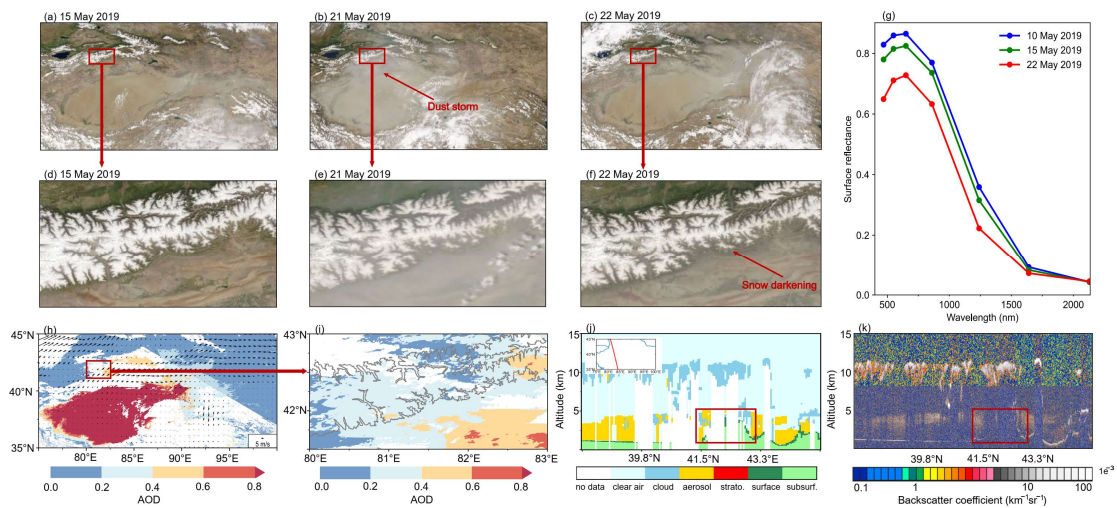
337

338 **Figure 3. Mountain ranges surrounding the Taklamakan Desert, and AOD and**  
 339 **dust deposition distributions across the Taklamakan Desert and surrounding**  
 340 **region. (a, b) Geographic location of the Taklamakan Desert and surrounding**  
 341 **mountains. The red box defines the area in (b). Spatial distributions of the**  
 342 **averaged (c) AOD and (d) dust deposition values, which were derived from**  
 343 **MCD19A2 and MERRA-2 during the March to August 2019 period.**

### 344 **3.1.1 Dust-induced snow darkening across the Tien Shan**

345 A significant dust storm occurred across the TD region on 18–22 May 2019 (Figures 4  
 346 and S2). The 21 May 2019 Terra/MODIS satellite image (Figure 4b) showed that the  
 347 dust plumes had spread to the north and east owing to an upper anticyclone system in  
 348 the Tarim Basin (Figure 4h). Some dust particles were uplifted to  $>4$  km altitude, as  
 349 shown in the CALIPSO aerosol vertical profiles (Figures 4j and k). These dust particles  
 350 were then transported to the snow-covered high-elevation areas of the Tien Shan, as  
 351 illustrated in the MODIS AOD images (Figures 4h and i). Dust plumes were also  
 352 observed in a satellite image that spanned the broadly snow-covered central Tien Shan  
 353 (Figure 4e), and the snow appeared to darken in the 22 May 2019 Terra/MODIS satellite  
 354 image that was acquired under the first clear-sky conditions after this severe dust event.  
 355 However, the snow was much whiter prior to the passage of this dust storm, as shown  
 356 in Figures 4d and f. Figure 4g further illustrates changes in the surface reflectance of

357 the snow-covered areas, providing a more intuitive influence of dust deposition on the  
 358 snow physical properties. The reflectance was around 0.8 in the VIS spectrum on 15  
 359 May 2019, but quickly decreased to  $<0.7$  on 22 May 2019, after the passage of the dust  
 360 plumes. The reduction in VIS wavelengths was up to  $>0.1$  during this short time interval.  
 361 These observations show that the dust plumes from the TD can significantly darken the  
 362 snowpack across the Tien Shan through heavy dust deposition. Furthermore, the  
 363 progression of air-temperature-induced snow aging cannot effectively explain this  
 364 phenomenon. This result is consistent with previous satellite observations over the  
 365 Himalayas (Gautam et al., 2013).

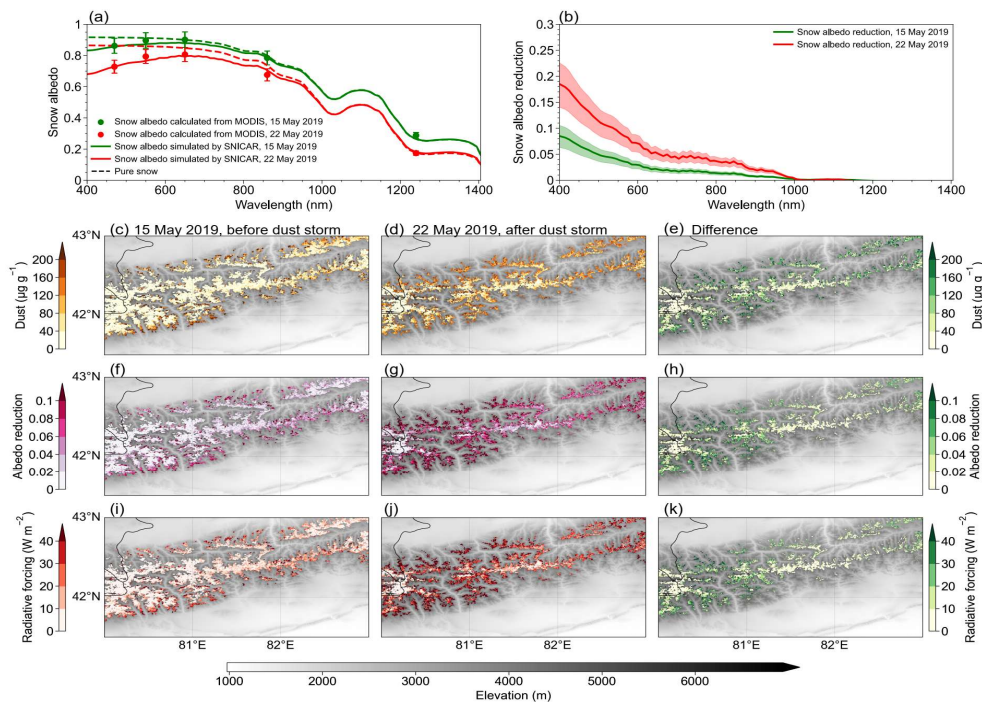


366

367 **Figure 4. Satellite observations during the 18–22 May 2019 severe dust event**  
 368 **across the Tien Shan. (a, d) Terra/MODIS satellite true-color images acquired on**  
 369 **15 May 2019, prior to the dust storm. (b, e) Terra/MODIS satellite images**  
 370 **acquired on 21 May 2019, with the dust storm transport from the TD to the Tien**  
 371 **Shan indicated by the red arrow in (b). (c, f) Terra/MODIS satellite images**  
 372 **acquired on 22 May 2019, with significant snow darkening observed across the**  
 373 **Tien Shan after the dust storm. (g) MOD09GA spectral surface reflectance across**  
 374 **snow-covered areas on 10 May 2019 (blue), 15 May 2019 (green), and 22 May 2019**  
 375 **(red). (h) MODIS AOD image on 21 May 2019, with the ERA5 daily mean wind**  
 376 **vector at 700 hPa overlain. (i) MODIS AOD image across the Tien Shan on 21**  
 377 **May 2019. Gray lines denote the 3000 m elevation contour. CALIPSO (j) vertical**  
 378 **feature mask and (k) backscatter coefficient on 21 May 2019.**



379 We also derived the spectral snow albedo and retrieved several parameters to  
380 quantitatively assess the impact of this dust deposition on snow darkening. The  
381 SNICAR-simulated spectral snow albedo (solid lines) and MODIS-derived 5-band  
382 snow albedo (dots) in Figure 5a are averaged over the area in Figure 5c. These results  
383 demonstrate an agreement of >95%, thereby indicating the reliability of our retrievals.  
384 The spectral snow albedo reduction on 15 and 22 May 2019 are shown in Figure 5b.  
385 There were significant increases in the albedo reductions as the wavelength decreased,  
386 particularly on 22 May 2019, which is consistent with theoretical simulations of the  
387 dust-induced snow darkening effect (Figure 1). However, the spectral curve differed  
388 from the BC-induced results in the anthropogenically influenced areas of Northeast  
389 China (Wang et al., 2017; Niu et al., 2022) and Northwest China (Shi et al., 2020).  
390 Therefore, we indicate that the observed snow darkening in this study was mainly  
391 caused by natural dust emissions, as opposed to BC and organic carbon (OC) emissions  
392 from anthropogenic activities and/or biomass burning. There was a spectral snow  
393 albedo reduction of 0.02–0.08 in the VIS on 15 May 2019, which represents persistent  
394 but relatively low dust deposition during spring. However, the severe dust event caused  
395 a rapid increase in spectral snow albedo reduction to 0.045–0.18 in a matter of days.  
396 The approximate doubling of the albedo reduction indicates that the increase in the dust  
397 concentration was much greater than 100% based on the nonlinear theory of the snow  
398 albedo feedback to the dust concentration (Figure 1). This implies that it is important  
399 to consider both the frequency and intensity of dust events when examining their impact  
400 on snow albedo. Similar phenomena that were induced by catastrophic wildfire events  
401 have been observed in the snowpack across New Zealand (Pu et al., 2021). These results  
402 suggest that extreme events may reflect the more pronounced impact of climate  
403 warming on our planet (Liang et al., 2021; Gui et al., 2022). Therefore, it is important  
404 to pay more attention to extreme events, rather than just conducting either annual or  
405 monthly averaged analyses, to fully capture the influence of climate change on snow  
406 albedo.



407

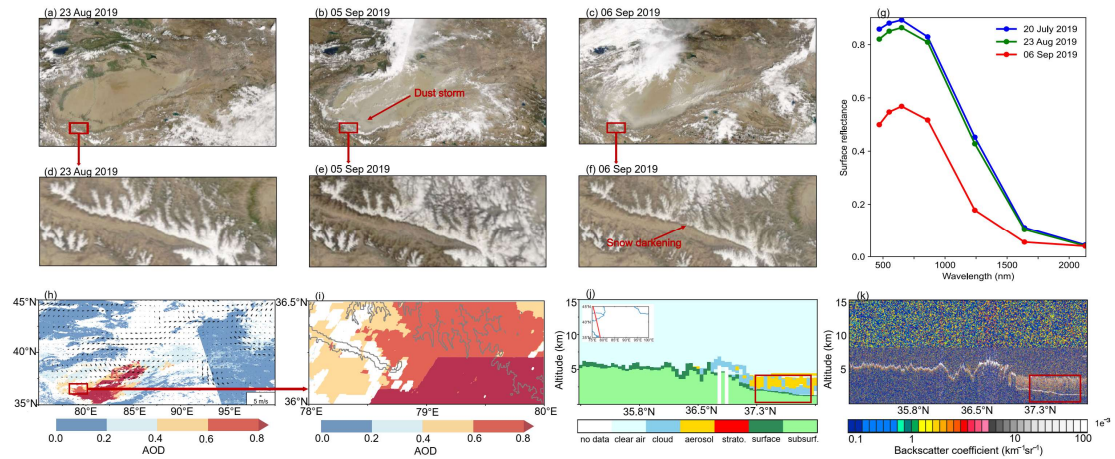
408 **Figure 5. (a) Averaged SNICAR-simulated spectral snow albedo (solid lines) and**  
 409 **MODIS-derived 5-band snow albedo (dots) for the region across the Tien Shan**  
 410 **impacted by the 18–22 May 2019 severe dust event. (b) Snow albedo reduction on**  
 411 **15 May 2019 (green) and 22 May 2019 (red). Shadows indicate the retrieval**  
 412 **uncertainty. Spatial distributions of the average (c, d) dust, (f, g) albedo reduction,**  
 413 **and (i, j) radiative forcing on 15 and 22 May 2019, respectively. Spatial**  
 414 **distributions of the differences in (e) dust, (h) albedo reduction, and (k) radiative**  
 415 **forcing between 15 and 22 May 2019. The background image in (c–k) is a grayscale**  
 416 **topographic map of the Tien Shan.**

417 Figures 5c and d illustrate the spatial distributions of the dust concentration in the  
 418 snowpack on 15 and 22 May 2019, respectively. There was a sharp increase in the dust  
 419 content from 2–55 to 42–192  $\mu\text{g g}^{-1}$  (~2.67-fold increase) following the severe dust  
 420 event, with the lower elevations possessing higher dust concentrations and greater dust  
 421 content increases (Figures 5d, 5e and S3). Snow darkening was observed across all of  
 422 the snow-covered areas ( $>2100 \text{ km}^2$ ), including the summits, thereby highlighting the  
 423 extensive influence of this severe dust event across the central Tien Shan. Furthermore,  
 424 these results demonstrate the capability and effectiveness of employing satellite remote  
 425 sensing to observe/monitor large-scale snow darkening. The dust-induced broadband

426 snow albedo reductions and radiative forcing are shown in Figures 5f–k, with observed  
427 spatial patterns that are largely similar to the dust content distributions. The snow  
428 albedo reduction increased by 0.008–0.052, with an observed increase from 0.002–  
429 0.032 on 15 May to 0.028–0.079 on 22 May. The radiative forcing increased by 2.5–  
430 20.5 W m<sup>-2</sup>, with an observed increase from 0.5–12.5 W m<sup>-2</sup> on 15 May to 11–31.5 W  
431 m<sup>-2</sup> on 22 May (Figure S4). Both the snow albedo reduction and radiative forcing  
432 increased by a factor of ~2.39, which directly reflects its significant impact on the  
433 regional radiation balance and climate (Dumont et al., 2020). Snow darkening can also  
434 accelerate snow aging by absorbing more shortwave radiation in a warming spring, as  
435 characterized by the R<sub>eff</sub> growth (Figures S3a–c). Figure S5a-d show the overall  
436 uncertainty in snow albedo reduction retrieval in Tien Shan, with the uncertainty  
437 bounds averaging 24% (-26%) on 15 May and 22% (-24%) on 22 May, respectively.  
438 As the dust content increases, the uncertainty in the snow albedo reduction decreases.

### 439 **3.1.2 Dust-induced snow darkening across the Kunlun Mountains**

440 The Kunlun Mountains are located along the southern (northern) edge of the Tarim  
441 Basin (Tibetan Plateau). The northern slope of the Central/West Kunlun Mountains  
442 directly faces the TD (Figure 1a) and should have experienced the most severe dust-  
443 induced snow darkening. Similar conditions also exist across the Himalayas, where the  
444 south slope faces both the Thar Desert in India and the Middle East. We captured a  
445 typical dust storm event with associated dust deposition and snow darkening that  
446 occurred between 5 and 11 May 2020 along the northern slope of the Kunlun Mountains  
447 using MODIS satellite images (Figure S6). The previously mentioned spring  
448 phenomenon is well-known due to intense springtime dust emissions from the TD,  
449 whereas the summer phenomenon is usually overlooked. However, it has been shown  
450 that dust can more effectively cross the Kunlun Mountains during the summer months,  
451 with the potential to induce changes in atmospheric dynamics and thermal effects (Yuan  
452 et al., 2018). Therefore, we specifically chose a summer case to highlight snow  
453 darkening across the Kunlun Mountains.

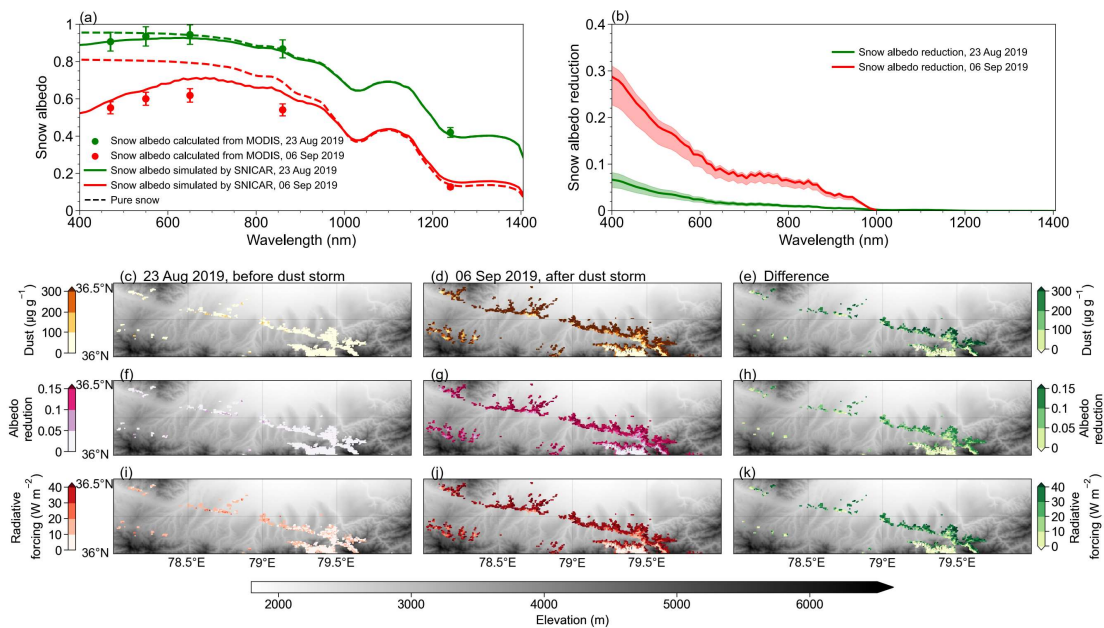


454

455 **Figure 6. Satellite observations during the 26 Aug to 08 Sep 2019 dust storm across**  
 456 **the Kunlun Mountains. (a, d) Terra/MODIS satellite true-color images acquired**  
 457 **on 23 Aug 2019, prior to the dust storm. (b, e) Terra/MODIS satellite images**  
 458 **acquired on 05 Sep 2019, with the dust storm transport from the TD to the Kunlun**  
 459 **Mountains indicated by the red arrow in (b). (c, f) Terra/MODIS satellite images**  
 460 **acquired on 06 Sep 2019, with significant snow darkening across the Kunlun**  
 461 **Mountains after the dust storm. (g) MOD09GA spectral surface reflectance over**  
 462 **the snow-covered areas on 20 July 2019 (blue), 23 Aug 2019 (green), and 06 Sep**  
 463 **2019 (red). (h) MODIS AOD image on 05 Sep 2019, with the ERA5 daily mean**  
 464 **wind vector at 700 hPa overlain. (i) MODIS AOD image across the Kunlun**  
 465 **Mountains on 05 Sep 2019. Gray lines denote the 3000-m elevation contour.**  
 466 **CALIPSO (j) vertical feature mask and (k) backscatter coefficient on 04 Sep 2019.**

467 A significant dust event that impacted the northern slope of the Kunlun Mountains  
 468 occurred from 26 Aug to 08 Sep 2019 (Figures 6b and S7). The Terra/MODIS satellite  
 469 images on 5 Sep 2019 (Figures 6b and e) show the accumulation of dust plumes along  
 470 the southern edge of the Tarim Basin. In summer, the westerlies weaken and shift to  
 471 the north, leading to more accumulation of dust locally instead of transporting it  
 472 eastward (Chen et al., 2017a; Yuan et al., 2018). Furthermore, the enhanced sensible  
 473 heat flux favors the southward transport of uplifted dust, leading to cyclonic  
 474 convergence at the surface and anticyclonic divergence at the top of the troposphere  
 475 above the TD (Figure 6h). The synergistic effects of atmospheric dynamic and thermal

476 forcing can cause the dust plumes to be uplifted to  $\sim 5$  km altitude (Figures 6j–k). This  
 477 uplift effectively facilitated the dust plume ascent to the snow-covered areas across the  
 478 northern slope of the Kunlun Mountains (Figure 6e and i). A comparison of the MODIS  
 479 images that were acquired on 23 Aug and 6 Sep 2019 highlighted snow darkening after  
 480 this severe dust storm (Figures 6d and f). The surface reflectance decreased by  $\sim 0.22$   
 481 in the VIS spectrum, decreasing from 0.285 on 23 Aug to  $\sim 0.065$  on 5 Sep. These  
 482 observations indicate that this summertime dust event caused significant snow  
 483 darkening across the Kunlun Mountains.



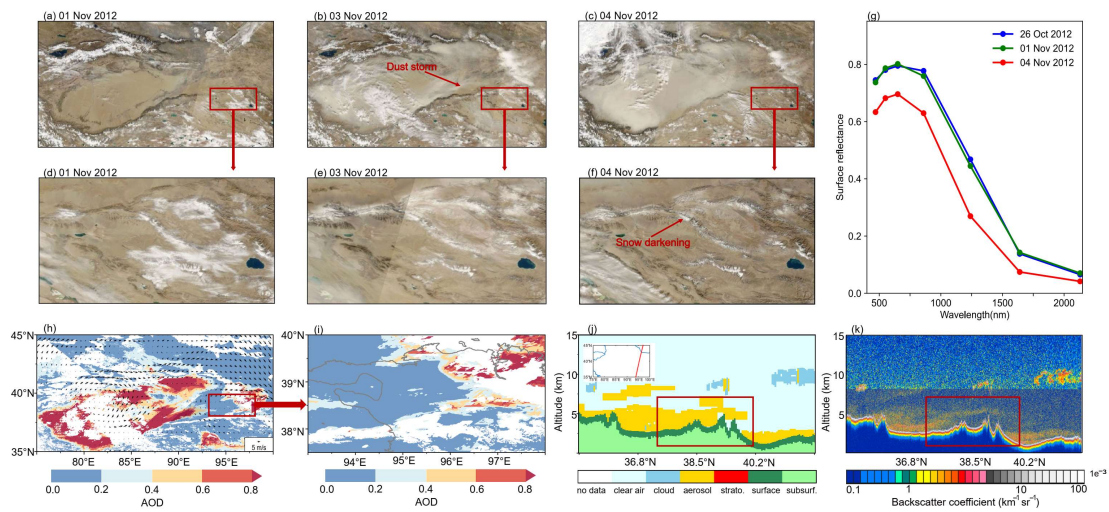
484  
 485 **Figure 7. (a) Averaged SNICAR-simulated spectral snow albedo (solid lines) and**  
 486 **MODIS-derived 5-band snow albedo (dots) for the region across the Kunlun**  
 487 **Mountains impacted by the 26 Aug to 08 Sep 2019 severe dust event. (b) Snow**  
 488 **albedo reductions on 23 Aug 2019 (green) and 06 Sep 2019 (red). Shadows indicate**  
 489 **the retrieval uncertainty. Spatial distributions of the average (c, d) dust, (f, g)**  
 490 **albedo reduction, and (€, j) radiative forcing on 23 Aug and 06 Sep 2019,**  
 491 **respectively. Spatial distributions of the differences in€) dust, (h) albedo reduction,**  
 492 **and (k) radiative forcing between 23 Aug and 06 Sep 2019. The background image**  
 493 **in (c–k) is a grayscale topographic map of the Kunlun Mountains.**

494 Figure 7 provides a more quantitative investigation of the impact of this severe dust  
 495 event on the snowpack across the Kunlun Mountains, whereby a significant increase in

496 dust content from 12–50  $\mu\text{g g}^{-1}$  on 23 Aug to 170–360  $\mu\text{g g}^{-1}$  on 06 Sep (~6.45-fold  
497 increase) is observed after this severe dust event (Figure S8). The darkened snow-  
498 covered area spans  $>600 \text{ km}^2$ , with a clear south–north gradient in the dust  
499 concentration distribution that is influenced by both the orientation and elevation of the  
500 mountains. This large dust deposition induced a 0.015–0.106 increase in snow albedo  
501 reduction, with an observed increase from 0.013–0.032 on 23 Aug to 0.088–0.136 on  
502 06 Sep. There was also a substantial increase in radiative forcing of 4.1–37.5  $\text{W m}^{-2}$ ,  
503 with an observed increase from 3–11  $\text{W m}^{-2}$  on 23 Aug to 31–49  $\text{W m}^{-2}$  on 06 Sep  
504 (Figure S4). Note that these increases in both the snow albedo reduction and radiative  
505 forcing are approximately two times larger than those observed over the Tien Shan  
506 (Figure S3 and S8). These findings indicate accelerated snow aging, as evidenced by  
507 the faster growth rate of the  $R_{\text{eff}}$  observed across the Kunlun Mountains (Figures S9).  
508 Furthermore, Figure S5e-h show the overall uncertainty in snow albedo reduction  
509 retrieval in Kunlun Mountains, with the uncertainty bounds averaging 23% (-25%) on  
510 23 Aug and 7% (-21%) on 06 Sep, respectively. Notably, compared to the Tien Shan  
511 dust event described in Section 3.1.1, the Kunlun Mountains event demonstrates a more  
512 significant reduction in the uncertainty of snow albedo reduction as the dust content  
513 increases, especially in the upper bound of the uncertainty. This observation aligns with  
514 findings reported by Cui et al. (2021).

### 515 **3.1.3 Snow darkening across the Qilian Mountains**

516 Unlike the Tien Shan and Kunlun Mountains, the Qilian Mountains are located  
517 approximately 1000 km east of the Tarim Basin. The Hexi Corridor, a narrow and  
518 relatively flat plain that lies between the high-elevation, inhospitable terrains of the  
519 Mongolian and Tibetan plateaus (see Figure 3), is situated to the north of the Qilian  
520 Mountains. The unique terrain of the region results in TD dust plumes following a  
521 preferred transport route across the Hexi Corridor to East Asia (Zhang et al., 2008;  
522 Meng et al., 2018). These dust plumes are generally uplifted to  $>4 \text{ km}$  altitude and  
523 entrained in the westerlies (Huang et al., 2008; Dong et al., 2014; Chen et al., 2022),  
524 thereby providing a means for dust deposition onto the snowpack across the Qilian  
525 Mountains.

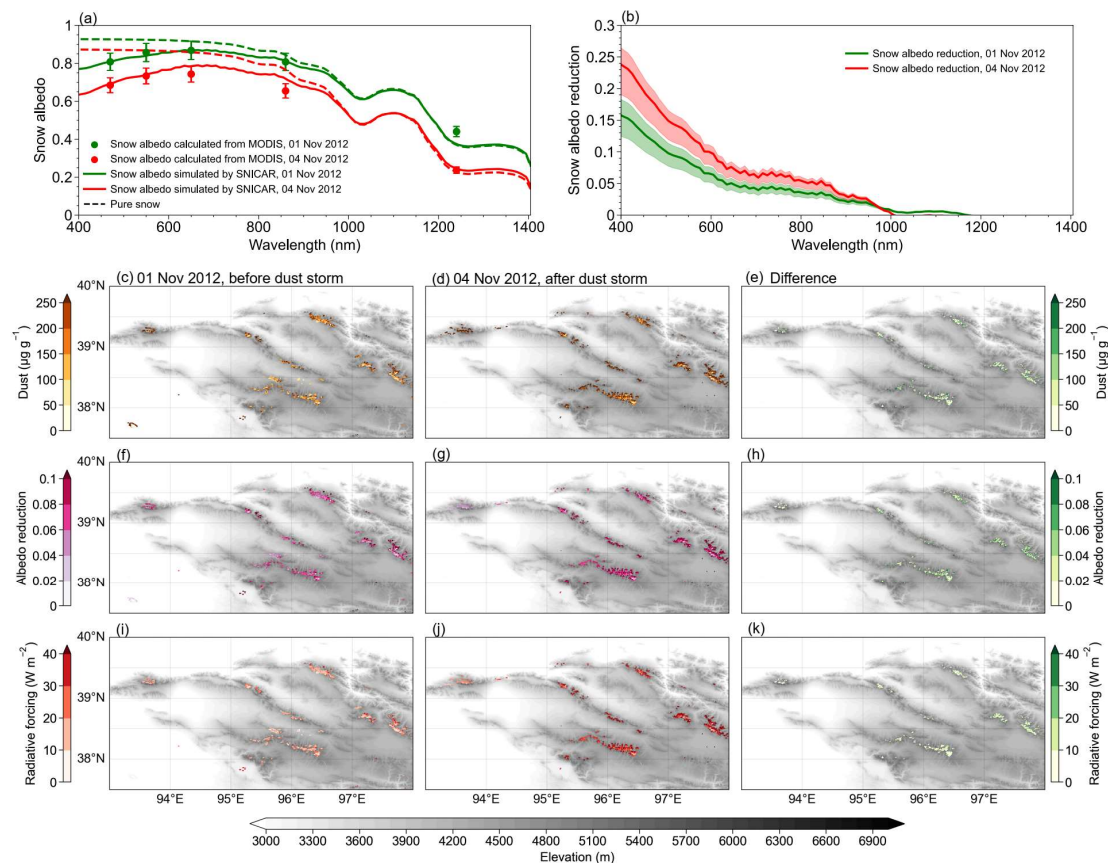


527

528 **Figure 8. Satellite observations during the 02–04 Nov 2012 dust storm across the**  
 529 **Qilian Mountains. (a, d) Terra/MODIS satellite true-color images acquired on 01**  
 530 **Nov 2012, prior to the dust storm. (b, e) Terra/MODIS satellite images acquired**  
 531 **on 03 Nov 2012, with the dust transport from the TD to the Qilian Mountains**  
 532 **indicated by the red arrow in (b). (c, f) Terra/MODIS satellite images acquired on**  
 533 **04 Nov 2012, with significant snow darkening observed across the Qilian**  
 534 **Mountains after the dust storm. (g) MOD09GA spectral surface reflectance over**  
 535 **the snow-covered areas on 26 Oct 2012 (blue), 01 Nov 2012 (green), and 04 Nov**  
 536 **2012 (red). (h) MODIS AOD image on 03 Nov 2012, with the ERA5 daily mean**  
 537 **wind vector at 700 hPa overlain. (i) MODIS AOD image across the Qilian**  
 538 **Mountains on 03 Nov 2012. The gray line denotes the 3000-m elevation contour.**  
 539 **CALIPSO (j) vertical feature mask and (k) backscatter coefficient on 03 Nov 2012.**

540 Figure 8 illustrates a severe dust event that occurred from 02 to 04 Nov 2012 (Figure  
 541 S10), when abundant dust plumes were being transported across the narrow Hexi  
 542 Corridor (Figures 8b and h). The dust content was much more intense in this region,  
 543 possessing AOD levels of up to  $>0.8$ . Furthermore, the CALIPSO observations  
 544 indicated that the dust plumes were uplifted to  $\sim 10$  km altitude (Figures 8j and k),  
 545 thereby allowing some dust particles to cross over the northern slopes of the Qilian  
 546 Mountains and spread across its western extent (Figures 8e and i). The average

547 reflectance in the VIS spectrum was stable at around 0.7–0.8 across the snow-covered  
 548 areas about a week before the severe dust event but then significantly decreased to  
 549 0.6–0.7 owing to heavy dust deposition



550  
 551 **Figure 9. (a) Averaged SNICAR-simulated spectral snow albedo (solid lines) and**  
 552 **MODIS-derived 5-band snow albedo (dots) for the region across the Qilian**  
 553 **Mountains impacted by the 02–04 Nov 2012 severe dust event. (b) Snow albedo**  
 554 **reductions on 01 Nov 2012 (green) and 04 Nov 2012 (red). Shadows indicate the**  
 555 **retrieval uncertainty. Spatial distributions of the average (c, d) dust, (f, g) albedo**  
 556 **reduction, and (i, j) radiative forcing on 01 and 04 Nov 2012, respectively. Spatial**  
 557 **distributions of the differences in (e) dust, (h) albedo reduction, and (k) radiative**  
 558 **forcing between 01 and 04 Nov 2012. The background image in (c–k) is a grayscale**  
 559 **image of the Qilian Mountains.**

560 Figure 9 presents the quantitative satellite-derived results, which highlight a rapid  
 561 increase in dust content from 110–228 to 194–360  $\mu\text{g g}^{-1}$  (~1.53-fold increase) that  
 562 spanned a snow-covered area of  $>630 \text{ km}^2$  (Figures 9f–h). This significant increase in

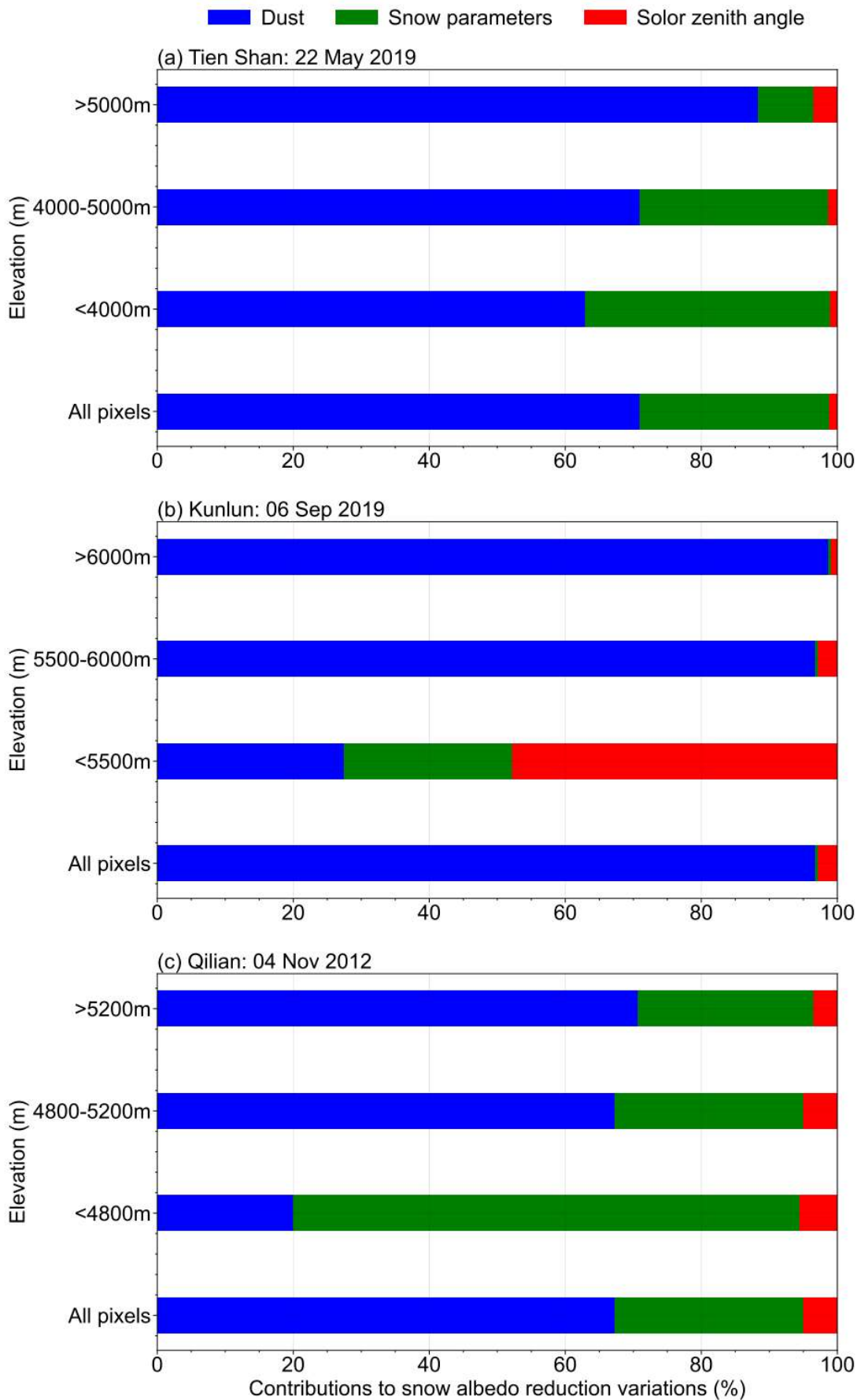


563 dust content led to a considerable increase in snow albedo reduction (radiative forcing)  
564 of 0.018–0.067 (3–16 W m<sup>-2</sup>), which increased from 0.042–0.076 (11–20 W m<sup>-2</sup>) on 1  
565 Nov 2012 to 0.092–0.153 (22–38 W m<sup>-2</sup>) on 4 Nov 2012 (Figure S4). This >1.5-fold  
566 increase in snow albedo reduction (radiative forcing) was not solely due to the  
567 deposition of dust (Figure S11). Accelerated snow aging, which was observed from the  
568 enhanced R<sub>eff</sub> growth (Figure S9), also contributed to the observed increase in snow  
569 albedo reduction (radiative forcing); this trend was similar to that observed across the  
570 Kunlun Mountains. Figure S5i-l show the overall uncertainty in snow albedo reduction  
571 retrieval in Qilian Mountains, with the uncertainty bounds averaging 16% (-21%) on  
572 01 Nov and 11% (-20%) on 04 Nov, respectively. Our approach uses satellite remote  
573 sensing to obtain a more complete spatiotemporal evolution of the TD dust storm,  
574 including its emission, long-range transport, and deposition, across the Qilian  
575 Mountains, which offers advantages over previous field measurements (Wei et al.,  
576 2017).

### 577 **3.2 Contributions to the spatial and altitudinal variations in dust-induced snow** 578 **darkening**

579 We quantified the contributions of the three key factors (dust content, snow properties,  
580 and solar zenith) to the spatial variations in snow albedo reduction (Figure 10) using  
581 the method described in Section 2.6. The dust content was the dominant contributor to  
582 the spatial variations in snow darkening. This is at least partially attributed to the greater  
583 spatial differences in dust content compared with those of the other factors, as shown  
584 in Figures 5, 7, and 9. Furthermore, theoretical modeling has indicated that the snow  
585 albedo reduction is more sensitive to changes in dust content than to changes in the  
586 snow properties and solar zenith angle (Flanner et al., 2021; Usha et al., 2022; Zhao et  
587 al., 2022). Laboratory experiments also support these findings (Zhang et al., 2018; Li  
588 et al., 2022). The contribution of the dust content also increased as the elevation in each  
589 mountain range increased, whereas a decreasing trend was observed for the snow  
590 parameters. This is because the dust content exhibits spatial differences across all of the  
591 elevations owing to its widespread and heterogeneous depositions. However, the snow  
592 depth has a more semi-infinite nature and R<sub>eff</sub> exhibits greater spatial homogeneity at

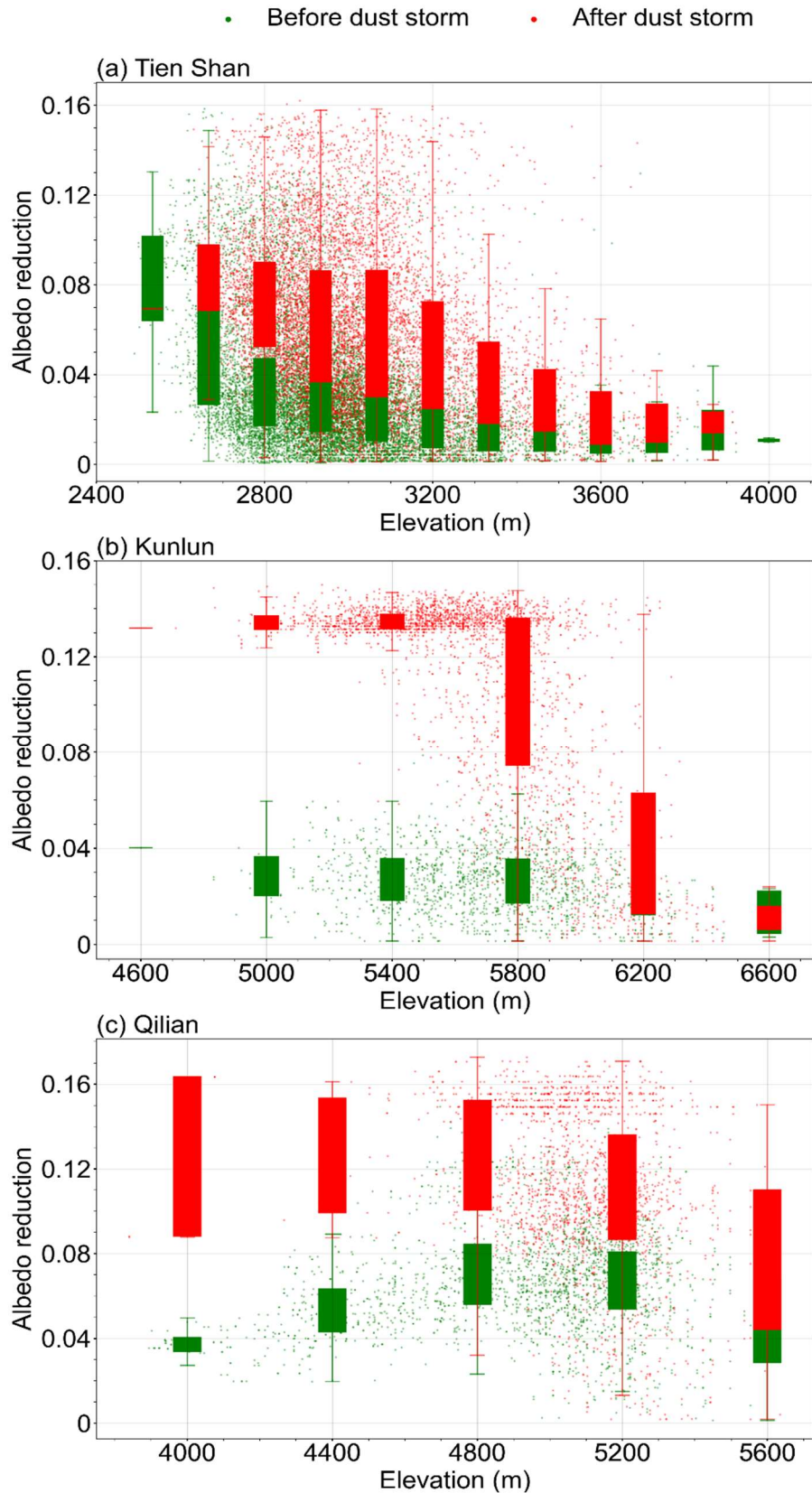
593 higher elevations owing to slower snow aging.



594

595 **Figure 10. Contributions of the spatial variations in dust content (blue), snow**  
596 **parameters (green), and solar zenith angle (red) to the snow albedo reduction at**  
597 **different elevations across the (a) Tien Shan, (b) Kunlun Mountains, and (c) Qilian**  
598 **Mountains.**

599 Scatter plots of the snow albedo reduction for the elevations across the Tien Shan,  
600 Kunlun Mountains, and Qilian Mountains are shown in Figure 11. The snow albedo  
601 reduction across the Tien Shan decreased with increasing elevation prior to the dust  
602 storm. However, the most severe dust deposition occurred within the 4000–4500 m  
603 elevation range, resulting in the most significant enhancement of snow albedo reduction  
604 in this elevation range. These findings are consistent with those reported for the  
605 Himalayas (Sarangi et al., 2020). The snow albedo reduction was generally low across  
606 the Kunlun Mountains for all of the elevation ranges. However, dust deposition caused  
607 the most significant albedo reduction within the 4500–5500 m elevation range, with a  
608 dramatic decrease of its influence above 6000 m. These findings correspond to the  
609 CALIPSO aerosol vertical profile observations (Figures 6j and k). The snow albedo  
610 reduction across the Qilian Mountains initially increased with elevation up to ~5000 m  
611 and then decreased at high elevations prior to the dust storm. However, the most severe  
612 dust deposition occurred across the lower elevations, leading to the most significant  
613 enhancement of snow albedo reduction across these lower-elevation regions. Our  
614 elevation analysis revealed a consistent outcome, whereby the dust storms significantly  
615 darkened the snowpack up to >5000 m elevation across the three analyzed mountain  
616 ranges.



617

618 **Figure 11. Scatter plots of the snow albedo reductions for the analyzed elevation**

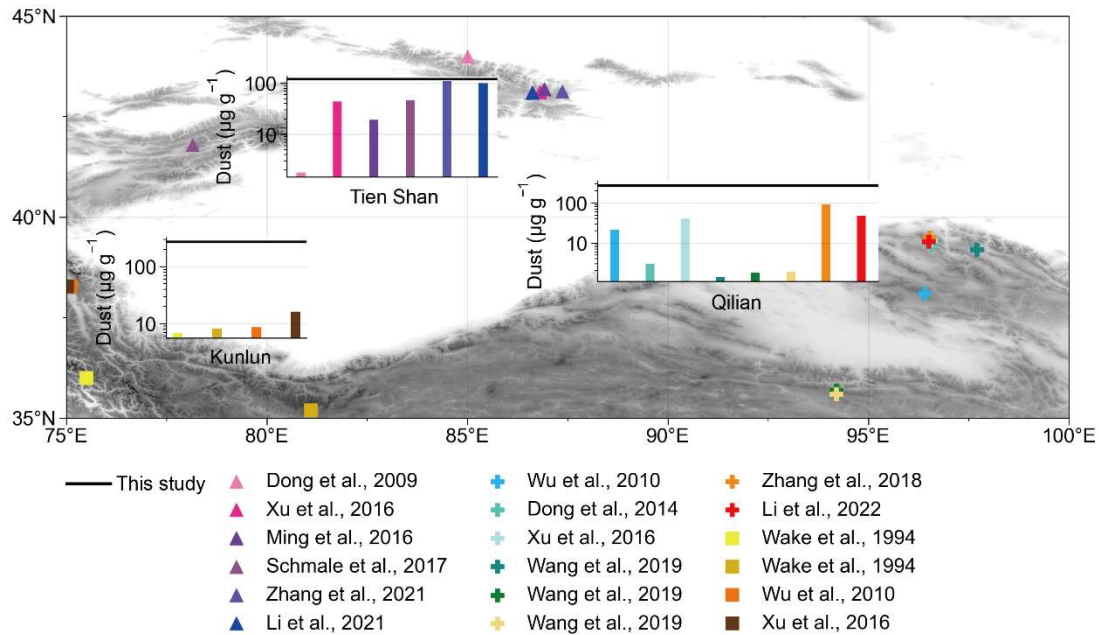
619 **ranges across the (a) Tien Shan, (b) Kunlun Mountains, and (c) Qilian Mountains.**

620 **Each box plot shows the statistical results for a 400-m elevation interval.**

## 621 **4 Discussion**

622 The snow darkening effect and its resultant radiative forcing have gained increasing  
623 attention in recent decades owing to their significant impacts on regional climate and  
624 hydrological systems. However, studies in the Tien Shan, Kunlun Mountains, and  
625 Qilian Mountains have been limited to local-scale observations, despite the significant  
626 impact of dust on snow darkening in these regions. Here we provide an overview of  
627 previous in situ dust-content measurements in the snowpack across the study region for  
628 comparison with our satellite remote-sensing results (see Figure 12). In the Tien Shan  
629 region, Ming et al. (2016), Xu et al. (2016), Li et al. (2021), and Zhang et al. (2021)  
630 reported a dust content of 19.3–110  $\mu\text{g g}^{-1}$  in the snowpack across Urumqi Glacier No.1.  
631 Dong et al. (2009) observed an average dust content of 0.97–3.69  $\mu\text{g g}^{-1}$  in the  
632 snowpack across Urumqi Glacier No. 1, Haxilegen Glacier No. 51, and Miaoergou  
633 Glacier. Schmale et al. (2017) found a variable dust content of 68.1–125.9  $\mu\text{g g}^{-1}$  in the  
634 snowpack across Suet Zapadniy, No. 354, and Golubin glaciers in the western Tien  
635 Shan. In the Kunlun Mountains, Wake et al. (1994) reported a dust content of up to  $\sim 8$   
636  $\mu\text{g g}^{-1}$  in the snow/ice across the western Kunlun Mountains. Wu et al. (2010) and Xu  
637 et al. (2016) measured dust contents of  $\sim 8.68$  and  $16.24 \mu\text{g g}^{-1}$  in the ice core and  
638 snowpack across Muztagata Glacier in the northwestern Tibet Plateau (Wu et al., 2010;  
639 Xu et al., 2016), respectively. In the Qilian Mountains, Wu et al. (2010) analyzed ice  
640 cores from Dunde Glacier and measured a dust content of  $\sim 21 \mu\text{g g}^{-1}$ . The measured  
641 dust contents in the snowpack across Laohugou Glacier ranged from around 3 to 93.2  
642  $\mu\text{g g}^{-1}$  (Dong et al., 2014; Xu et al., 2016; Zhang et al., 2018; Li et al., 2022). Wang et  
643 al. (2019) measured a variable dust content of 1.4–1.9  $\mu\text{g g}^{-1}$  in the fresh snow across  
644 Qiyi, Meikuang, and Yuzhufeng glaciers. Overall, previous field studies have reported  
645 dust contents of 0.97–125.9, 6.78–16.24, and 1.4–93.2  $\mu\text{g g}^{-1}$  for the Tien Shan, Kunlun  
646 Mountains, and Qilian Mountains, respectively.

647



648

649

**Figure 12. Comparisons of the satellite-derived dust contents (black lines) in snow from this study and observed values from previous studies (colored symbols and bars).**

650

651

652

Our satellite-derived approach has yielded much higher dust contents than those obtained via in situ field measurements, with 42–196, 170–360, and 194–360  $\mu\text{g g}^{-1}$  determined for the Tien Shan, Kunlun Mountains, and Qilian Mountains, respectively.

653

654

A key reason for this discrepancy could be that the field measurements usually record the background dust content signal, which includes a gradual natural deposition of dust, whereas our analysis specifically focused on significant snow darkening events due to severe dust storms, which further highlights the advantage of employing remote-sensing techniques to observe extreme snow darkening phenomena (Li et al., 2020).

655

656

657

658

659

660

661

662

663

664

665

666

667

We do note that satellite-derived approaches possess their own uncertainties, which arise from the data resolution and accuracy, algorithm assumptions, and atmospheric and underlying surface interferences (Cui et al., 2021). Nevertheless, this satellite-derived approach remains a valuable tool for effectively and rapidly studying extreme events, which cannot be captured by field measurements or climate model simulations, particularly as these extreme events will become increasingly important for climate and hydrological systems as the global climate continues to warm (Clow et al., 2016; Dumont et al., 2020).

668 Given the significant snow darkening effect highlighted in this study and recent  
669 observations of decreasing snow cover across the Tien Shan, Kunlun Mountains, and  
670 Qilian Mountains (She et al., 2015; Li et al., 2020; Zhu et al., 2022), it is crucial to  
671 evaluate the impact of snow darkening on regional hydrologic cycles and local  
672 freshwater supplies. However, snow aging and melting mechanisms are complex and  
673 therefore require complementary observations because remote sensing alone cannot  
674 distinguish the influences of augmented shortwave radiation owing to dust and  
675 increased air temperatures on snow aging and melting (Gautam et al., 2013). Additional  
676 research that integrates model simulations and satellite observations is necessary to  
677 differentiate the roles of snow darkening and global warming in enhancing snow aging  
678 and melting, and the resultant changes in glacier runoff in the future.

## 679 **5 Conclusions**

680 Our study focused on the impact of the annual vast dust emissions from the Taklamakan  
681 Desert on the surrounding high mountain snowpack. Using a combination of MODIS  
682 satellite data analysis and SNICAR model simulations, we aimed to reveal significant  
683 snow-darkening events and quantify the resulting snow albedo reduction and radiative  
684 forcing caused by severe dust storms. Our analysis of the satellite data revealed  
685 significant snow darkening over the 3000–6000 m elevation range across the Tien Shan  
686 and Kunlun Mountains. This phenomenon was attributed to the high uplift of dust  
687 owing to the local topography and atmospheric circulation. The impacted area,  
688 spanning the track of the dust storm, encompassed almost all of the snow-covered areas  
689 across the Tien Shan ( $>2100 \text{ km}^2$ ) and Kunlun Mountains ( $>600 \text{ km}^2$ ), including the  
690 summits. The dust content in the snowpack increased to 42–192 and 170–360  $\mu\text{g g}^{-1}$ ,  
691 resulting in significant increases in snow albedo reduction (radiative forcing) of 0.028–  
692 0.079 ( $11\text{--}31.5 \text{ W m}^{-2}$ ) and 0.088–0.136 ( $31\text{--}49 \text{ W m}^{-2}$ ) across the Tien Shan and  
693 Kunlun Mountains, respectively. Additionally, the dust storms accelerated snow aging,  
694 as indicated by the growth of  $R_{\text{eff}}$ . Furthermore, the dust plumes from the Taklamakan  
695 Desert traveled eastward, depositing dust across much of the snow-covered area ( $>630$   
696  $\text{km}^2$ ) in the Qilian Mountains, where the dust content significantly increased to 194–

697 360  $\mu\text{g g}^{-1}$ , causing a considerable increase in snow albedo reduction (radiative forcing)  
698 of 0.092–0.153 (22–38  $\text{W m}^{-2}$ ). The spatial distribution of the snow-darkening effect  
699 varied across all three mountain ranges due to the uneven deposition of dust, with the  
700 most significant snow darkening observed in the high elevation range of 4000–5500 m.  
701 Moreover, by comparing our satellite-derived results with previous field measurements,  
702 we found that severe dust storms, occurring over short periods, have a more profound  
703 effect on snow darkening compared with the relatively slow deposition of dust in the  
704 absence of dust storms. These severe snow darkening events were not limited to the  
705 three typical cases but occurred widely (Figures S13-S21). This highlights the  
706 importance of satellite-derived analyses in capturing extreme dust deposition events  
707 that may be challenging to detect through field measurements and climate model  
708 simulations. Our findings underscore the significance of understanding the impact of  
709 dust deposition on snow albedo and radiative forcing for accurate assessment of the  
710 environmental effects of these extreme events.

711

712

713

714

715

716

717

718

719

720

721



722 *Data availability.* All datasets and codes used to produce this study can be obtained by  
723 contacting Wei Pu (puwei@lzu.edu.cn).

724 *Author contributions.* WP and XW designed the study and developed the overarching  
725 research goals and aims. YX carried the study out and wrote the first draft with  
726 contributions from all co-authors. YX processed the data with the assistance of YC, SY,  
727 TS, XC, XN, DW, JC and YZ. WP and XW assumed oversight and leadership  
728 responsibility for the research activity planning and execution. All authors contributed  
729 to the improvement of results and revised the final paper.

730 *Competing interests.* The authors declare that they have no conflict of interest.

731 *Acknowledgements.* The Lanzhou University group acknowledges support from the  
732 National Science Fund for Distinguished Young Scholars, the State Key Laboratory of  
733 Cryosphere Science Open Fund and the National Natural Science Foundation of China.  
734 We appreciate Dr. Boyuan Zhang's assistance with the code improvements. We thank  
735 Lanzhou City's scientific research funding subsidy to Lanzhou University and the  
736 Supercomputing Center of Lanzhou University for providing the computing services.

737 *Financial support.* This research was supported by the National Science Fund for  
738 Distinguished Young Scholars (42025102), the State Key Laboratory of Cryosphere  
739 Science Open Fund (SKLCS-OP-2021-05) and the National Natural Science  
740 Foundation of China (42375068 and 42075061) and the Natural Science Foundation of  
741 Gansu province, China (21ZDKA0017).

742 **Reference**

- 743 Arun, B. S., Aswini, A. R., Gogoi, M. M., Hegde, P., Kumar Kompalli, S., Sharma, P.,  
744 and Suresh Babu, S.: Physico-chemical and optical properties of aerosols at a  
745 background site (~4 km a.s.l.) in the western Himalayas, *Atmospheric*  
746 *Environment*, 218, 10.1016/j.atmosenv.2019.117017, 2019.
- 747 Arun, B. S., Gogoi, M. M., Borgohain, A., Hegde, P., Kundu, S. S., and Babu, S. S.:  
748 Role of sulphate and carbonaceous aerosols on the radiative effects of aerosols  
749 over a remote high-altitude site Lachung in the Eastern Himalayas, *Atmospheric*  
750 *Research*, 263, 10.1016/j.atmosres.2021.105799, 2021a.
- 751 Arun, B. S., Gogoi, M. M., Hegde, P., Borgohain, A., Boreddy, S. K. R., Kundu, S. S.,  
752 and Babu, S. S.: Carbonaceous Aerosols over Lachung in the Eastern Himalayas:  
753 Primary Sources and Secondary Formation of Organic Aerosols in a Remote High-  
754 Altitude Environment, *ACS Earth and Space Chemistry*, 5, 2493-2506,  
755 10.1021/acsearthspacechem.1c00190, 2021b.
- 756 Bair, E. H., Stillinger, T., and Dozier, J.: Snow property inversion from remote sensing  
757 (SPIReS): A generalized multispectral unmixing approach with examples from  
758 MODIS and Landsat 8 OLI, *IEEE Transactions on Geoscience and Remote*  
759 *Sensing*, 59, 7270-7284, 10.1109/tgrs.2020.3040328, 2020.
- 760 Baladima, F., Thomas, J. L., Voisin, D., Dumont, M., Junquas, C., Kumar, R., Lavaysse,  
761 C., Marelle, L., Parrington, M., and Flemming, J.: Modeling an extreme dust  
762 deposition event to the French Alpine seasonal snowpack in April 2018:  
763 Meteorological context and predictions of dust deposition, *Journal of Geophysical*  
764 *Research: Atmospheres*, 127, 10.1029/2021jd035745, 2022.
- 765 Bormann, K. J., Brown, R. D., Derksen, C., Painter, T. H.: Estimating snow-cover  
766 trends from space, *Nature Climate Change*, 11, 924-928, 10.1038/s41558-018-  
767 0318-3, 2018.
- 768 Chaubey, J. P., Moorthy, K. K., Babu, S. S., Nair, V. S., and Tiwari, A.: Black carbon  
769 aerosols over coastal Antarctica and its scavenging by snow during the Southern  
770 Hemispheric summer, *Journal of Geophysical Research: Atmospheres*, 115,  
771 10.1029/2009jd013381, 2010.
- 772 Chen, B., Song, Z., Huang, J., Zhang, P., Hu, X., Zhang, X., Guan, X., Ge, J., and Zhou,  
773 X.: Estimation of atmospheric PM10 Concentration in China using an  
774 interpretable deep learning model and top-of-the-atmosphere reflectance data from  
775 China's new generation geostationary meteorological satellite, FY-4A, *Journal of*  
776 *Geophysical Research: Atmospheres*, 127, 10.1029/2021jd036393, 2022.
- 777 Chen, S., Huang, J., Zhao, C., Qian, Y., Leung, L. R., and Yang, B.: Modeling the  
778 transport and radiative forcing of Taklimakan dust over the Tibetan Plateau: A case  
779 study in the summer of 2006, *Journal of Geophysical Research: Atmospheres*, 118,  
780 797-812, 10.1002/jgrd.50122, 2013.
- 781 Chen, S., Huang, J., Li, J., Jia, R., Jiang, N., Kang, L., Ma, X., and Xie, T.: Comparison  
782 of dust emissions, transport, and deposition between the Taklimakan Desert and  
783 Gobi Desert from 2007 to 2011, *Science China Earth Sciences*, 60, 1338-1355,  
784 10.1007/s11430-016-9051-0, 2017a.
- 785 Chen, S., Huang, J., Kang, L., Wang, H., Ma, X., He, Y., Yuan, T., Yang, B., Huang, Z.,

786 and Zhang, G.: Emission, transport, and radiative effects of mineral dust from the  
787 Taklimakan and Gobi deserts: comparison of measurements and model results,  
788 Atmospheric Chemistry and Physics, 17, 2401-2421, 10.5194/acp-17-2401-2017,  
789 2017b.

790 Chen, W., Wang, X., Cui, J., Cao, X., Pu, W., Zheng, X., Ran, H., and Ding, J.: Radiative  
791 forcing of black carbon in seasonal snow of wintertime based on remote sensing  
792 over Xinjiang, China, Atmospheric Environment, 247,  
793 10.1016/j.atmosenv.2021.118204, 2021.

794 Clow, D. W., Williams, M. W., and Schuster, P. F.: Increasing aeolian dust deposition to  
795 snowpacks in the Rocky Mountains inferred from snowpack, wet deposition, and  
796 aerosol chemistry, Atmospheric Environment, 146, 183-194,  
797 10.1016/j.atmosenv.2016.06.076, 2016.

798 Cohen, J. and Rind, D.: The Effect of Snow Cover on the Climate, J. Climate, 4, 689–  
799 706, 10.1175/1520-0442(1991)004<0689:Teosco>2.0.Co;2, 1991.

800 Copernicus Climate Change Service: ERA5: Fifth generation of ECMWF atmospheric  
801 reanalysis of the global climate, Copernicus Climate Change Service Climate Data  
802 Store (CDS), 2017.

803 Cordero, R., Sepúlveda, E., Feron, S., Damiani, A., Fernandez, F., Neshyba, S., Rowe,  
804 P. M., Asencio, V., Carrasco, J., Alfonso, J. A., Llanillo, P., Wachter, P., Seckmeyer,  
805 G., Stepanova, M., Carrera, J. M., Jorquera, J., Wang, C., Malhotra, A., Dana, J.,  
806 Khan, A. L., and Casassa, G.: Black carbon footprint of human presence in  
807 Antarctica, Nature Communications, 13, 2041-1723, s41467-022-28560-w, 2022.

808 Cui, J., Shi, T., Zhou, Y., Wu, D., Wang, X., and Pu, W.: Satellite-based radiative forcing  
809 by light-absorbing particles in snow across the Northern Hemisphere,  
810 Atmospheric Chemistry and Physics, 21, 269-288, 10.5194/acp-21-269-2021,  
811 2021.

812 Dang, C., Warren, S. G., Fu, Q., Doherty, S. J., Sturm, M., and Su, J.: Measurements of  
813 light-absorbing particles in snow across the Arctic, North America, and China:  
814 Effects on surface albedo, Journal of Geophysical Research: Atmospheres, 122,  
815 10.1002/2017jd027070, 2017.

816 Di Mauro, B., Fava, F., Ferrero, L., Garzonio, R., Baccolo, G., Delmonte, B., and  
817 Colombo, R.: Mineral dust impact on snow radiative properties in the European  
818 Alps combining ground, UAV, and satellite observations, Journal of Geophysical  
819 Research: Atmospheres, 120, 6080-6097, 10.1002/2015jd023287, 2015.

820 Dong, Z., Li, Z., Wang, F., and Zhang, M.: Characteristics of atmospheric dust  
821 deposition in snow on the glaciers of the eastern Tien Shan, China, Journal of  
822 Glaciology, 55, 797-804, 10.3189/002214309790152393, 2009.

823 Dong, Z., Qin, D., Chen, J., Qin, X., Ren, J., Cui, X., Du, Z., and Kang, S.:  
824 Physicochemical impacts of dust particles on alpine glacier meltwater at the  
825 Laohugou Glacier basin in western Qilian Mountains, China, Science of the Total  
826 Environment, 493, 930-942, 10.1016/j.scitotenv.2014.06.025, 2014.

827 Dong, Z., Brahney, J., Kang, S., Elser, J., Wei, T., Jiao, X., and Shao, Y.: Aeolian dust  
828 transport, cycle and influences in high-elevation cryosphere of the Tibetan Plateau  
829 region: New evidences from alpine snow and ice, Earth-Science Reviews, 211,

830 10.1016/j.earscirev.2020.103408, 2020.

831 Dong, Q., Huang, Z., Li, W., Li, Z., Song, X., Liu, W., Wang, T., Bi, J., and Shi, J.:

832 Polarization lidar measurements of dust optical properties at the junction of the

833 Taklimakan Desert–Tibetan Plateau, *Remote Sensing*, 14, 10.3390/rs14030558,

834 2022.

835 Dumont, M., Brun, E., Picard, G., Michou, M., Libois, Q., Petit, J. R., Geyer, M., Morin,

836 S., and Josse, B.: Contribution of light-absorbing impurities in snow to

837 Greenland’s darkening since 2009, *Nature Geoscience*, 7, 509-512,

838 10.1038/ngeo2180, 2014.

839 Dumont, M., Tuzet, F., Gascoïn, S., Picard, G., Kutuzov, S., Lafaysse, M., Cluzet, B.,

840 Nheili, R., and Painter, T. H.: Accelerated snow melt in the Russian Caucasus

841 Mountains after the Saharan dust outbreak in March 2018, *Journal of Geophysical*

842 *Research: Earth Surface*, 125, 10.1029/2020jf005641, 2020.

843 Flanner, M. G., Zender, C. S., Randerson, J. T., and Rasch, P. J.: Present-day climate

844 forcing and response from black carbon in snow, *Journal of Geophysical Research*,

845 112, 10.1029/2006jd008003, 2007.

846 Flanner, M. G., Zender, C. S., Hess, P. G., Mahowald, N. M., Painter, T. H., Ramanathan,

847 V., and Rasch, P. J.: Springtime warming and reduced snow cover from

848 carbonaceous particles, *Atmospheric Chemistry and Physics*, 9, 2481–2497,

849 10.5194/acp-9-2481-2009, 2009.

850 Flanner, M. G., Arnheim, J. B., Cook, J. M., Dang, C., He, C., Huang, X., Singh, D.,

851 Skiles, S. M., Whicker, C. A., and Zender, C. S.: SNICAR-ADv3: a community

852 tool for modeling spectral snow albedo, *Geoscientific Model Development*, 14,

853 7673-7704, 10.5194/gmd-14-7673-2021, 2021.

854 Gautam, R., Hsu, N. C., Lau, W. K. M., and Yasunari, T. J.: Satellite observations of

855 desert dust-induced Himalayan snow darkening, *Geophysical Research Letters*, 40,

856 988-993, 10.1002/grl.50226, 2013.

857 Ge, J. M., Huang, J. P., Xu, C. P., Qi, Y. L., and Liu, H. Y.: Characteristics of Taklimakan

858 dust emission and distribution: A satellite and reanalysis field perspective, *Journal*

859 *of Geophysical Research: Atmospheres*, 119, 11,772-711,783,

860 10.1002/2014jd022280, 2014.

861 Gogoi, M. M., Babu, S. S., Pandey, S. K., Nair, V. S., Vaishya, A., Girach, I. A., and

862 Koushik, N.: Scavenging ratio of black carbon in the Arctic and the Antarctic,

863 *Polar Science*, 16, 10-22, 10.1016/j.polar.2018.03.002, 2018.

864 Gogoi M. M., Babu, S. S., Arun, B. S., Moorthy, K. K., Ajay, A., Ajay, P., Suryavanshi,

865 A., Borgohain, A., Guha, A., Shaikh, A., Pathak, B., Gharai, B., Ramasamy, B.,

866 Balakrishnaiah, G., Menon, H. B., Kuniyal, J. C., Krishnan, J., Gopal, K. R.,

867 Maheswari, M., Naja, M., Kaur, P., Bhuyan, P. K., Gupta, P., Singh, P., Srivastava,

868 P., Singh, R. S., Kumar, R., Rastogi, S., Kundu, S. S., Kompalli, S. K., Panda, S.,

869 Rao, T. C., Das, T., and Kant, Y.: Response of ambient BC concentration across

870 the Indian region to the nation-wide lockdown: results from the ARFINET

871 measurements of ISRO-GBP, *Current Science*, 120, 10.18520/cs/v120/i2/341-351,

872 2021a.

873 Gogoi, M. M., Pandey, S. K., Arun, B. S., Nair, V. S., Thakur, R. C., Chaubey, J. P.,

874 Tiwari, A., Manoj, M. R., Kompalli, S. K., Vaishya, A., Prijith, S. S., Hegde, P.,  
875 and Babu, S. S.: Long-term changes in aerosol radiative properties over Ny-  
876 Ålesund: Results from Indian scientific expeditions to the Arctic, *Polar Science*,  
877 30, 10.1016/j.polar.2021.100700, 2021b.

878 Gui, K., Yao, W., Che, H., An, L., Zheng, Y., Li, L., Zhao, H., Zhang, L., Zhong, J.,  
879 Wang, Y., and Zhang, X.: Record-breaking dust loading during two mega dust  
880 storm events over northern China in March 2021: aerosol optical and radiative  
881 properties and meteorological drivers, *Atmospheric Chemistry and Physics*, 22,  
882 7905-7932, 10.5194/acp-22-7905-2022, 2022.

883 Hadley, O. L. and Kirchstetter, T. W.: Black-carbon reduction of snow albedo, *Nat. Clim.*  
884 *Change*, 2, 437–440, 10.1038/nclimate1433, 2012.

885 Han, Y., Wang, T., Tang, J., Wang, C., Jian, B., Huang, Z., and Huang, J.: New insights  
886 into the Asian dust cycle derived from CALIPSO lidar measurements, *Remote*  
887 *Sensing of Environment*, 272, 10.1016/j.rse.2022.112906, 2022.

888 He, C., Takano, Y., Liou, K.-N., Yang, P., Li, Q., and Chen, F.: Impact of snow grain  
889 shape and black carbon–snow internal mixing on snow optical properties:  
890 Parameterizations for climate models, *Journal of Climate*, 30, 10019-10036,  
891 10.1175/jcli-d-17-0300.1, 2017.

892 He, C., Liou, K. N., Takano, Y., Yang, P., Qi, L., and Chen, F.: Impact of grain shape  
893 and multiple black carbon internal mixing on snow albedo: Parameterization and  
894 radiative effect analysis, *Journal of Geophysical Research: Atmospheres*, 123,  
895 1253-1268, 10.1002/2017jd027752, 2018.

896 Huang, H., Qian, Y., He, C., Bair, E. H., and Rittger, K.: Snow albedo feedbacks  
897 enhance snow impurity-induced radiative forcing in the Sierra Nevada,  
898 *Geophysical Research Letters*, 49, e2022GL098102, 10.1029/2022GL098102,  
899 2022.

900 Huang, J., Minnis, P., Yi, Y., Tang, Q., Wang, X., Hu, Y., Liu, Z., Ayers, K., Trepte, C.,  
901 and Winker, D.: Summer dust aerosols detected from CALIPSO over the Tibetan  
902 Plateau, *Geophysical Research Letters*, 34, 10.1029/2007gl029938, 2007.

903 Huang, J., Minnis, P., Chen, B., Huang, Z., Liu, Z., Zhao, Q., Yi, Y., and Ayers, J. K.:  
904 Long-range transport and vertical structure of Asian dust from CALIPSO and  
905 surface measurements during PACDEX, *Journal of Geophysical Research*, 113,  
906 10.1029/2008jd010620, 2008.

907 Huang, J., Wang, T., Wang, W., Li, Z., and Yan, H.: Climate effects of dust aerosols  
908 over East Asian arid and semiarid regions, *Journal of Geophysical Research:*  
909 *Atmospheres*, 119, 10.1002/2014jd021796, 2014.

910 Immerzeel, W. W. and Bierkens, M. F. P.: Asia's water balance, *Nature Geoscience*, 5,  
911 841-842, 10.1038/ngeo1643, 2012.

912 Jia, R., Liu, Y., Chen, B., Zhang, Z., and Huang, J.: Source and transportation of summer  
913 dust over the Tibetan Plateau, *Atmospheric Environment*, 123, 210-219,  
914 10.1016/j.atmosenv.2015.10.038, 2015.

915 Kang, L., Huang, J., Chen, S., and Wang, X.: Long-term trends of dust events over  
916 Tibetan Plateau during 1961–2010, *Atmospheric Environment*, 125, 188-198,  
917 10.1016/j.atmosenv.2015.10.085, 2016.

918 Kraaijenbrink, P. D. A., Bierkens, M. F. P., Lutz, A. F., and Immerzeel, W. W.: Impact  
919 of a global temperature rise of 1.5 degrees Celsius on Asia's glaciers, *Nature*, 549,  
920 257-260, 10.1038/nature23878, 2017.

921 Kraaijenbrink, P. D. A., Stigter, E. E., Yao, T., and Immerzeel, W. W.: Climate change  
922 decisive for Asia's snow meltwater supply, *Nature Climate Change*, 11, 591-597,  
923 10.1038/s41558-021-01074-x, 2021.

924 Li, Y., Chen, Y., and Li, Z.: Climate and topographic controls on snow phenology  
925 dynamics in the Tianshan Mountains, Central Asia, *Atmospheric Research*, 236,  
926 10.1016/j.atmosres.2019.104813, 2020.

927 Li, Y., Kang, S., Zhang, X., Chen, J., Schmale, J., Li, X., Zhang, Y., Niu, H., Li, Z., Qin,  
928 X., He, X., Yang, W., Zhang, G., Wang, S., Shao, L., and Tian, L.: Black carbon  
929 and dust in the Third Pole glaciers: Revaluated concentrations, mass absorption  
930 cross-sections and contributions to glacier ablation, *Science of the Total  
931 Environment*, 789, 147746, 10.1016/j.scitotenv.2021.147746, 2021.

932 Li, Y., Kang, S., Zhang, X., Li, C., Chen, J., Qin, X., Shao, L., and Tian, L.: Dust  
933 dominates the summer melting of glacier ablation zones on the northeastern  
934 Tibetan Plateau, *Science of the Total Environment*, 856, 159214,  
935 10.1016/j.scitotenv.2022.159214, 2022.

936 Liang, P., Chen, B., Yang, X., Liu, Q., Li, A., Mackenzie, L., and Zhang, D.: Revealing  
937 the dust transport processes of the 2021 mega dust storm event in northern China,  
938 *Science Bulletin*, 67, 21-24, 10.1016/j.scib.2021.08.014, 2021.

939 Ménégoz, M., Krinner, G., Balkanski, Y., Boucher, O., Cozic, A., Lim, S., Ginot, P., Laj,  
940 P., Gallée, H., Wagnon, P., Marinoni, A., and Jacobi, H. W.: Snow cover sensitivity  
941 to black carbon deposition in the Himalayas: from atmospheric and ice core  
942 measurements to regional climate simulations, *Atmospheric Chemistry and  
943 Physics*, 14, 4237-4249, 10.5194/acp-14-4237-2014, 2014.

944 Meng, L., Yang, X., Zhao, T., He, Q., Lu, H., Mamtimin, A., Huo, W., Yang, F., and Liu,  
945 C.: Modeling study on three-dimensional distribution of dust aerosols during a  
946 dust storm over the Tarim Basin, Northwest China, *Atmospheric Research*, 218,  
947 285-295, 10.1016/j.atmosres.2018.12.006, 2018.

948 Ming, J., Xiao, C. D., Wang, F. T., Li, Z. Q., and Li, Y. M.: Grey Tianshan Urumqi  
949 Glacier No.1 and light-absorbing impurities, *Environmental Science and Pollution  
950 Research*, 23, 9549-9558, 10.1007/s11356-016-6182-7, 2016.

951 Mishra, S. K., Hayse, J., Veselka, T., Yan, E., Kayastha, R. B., LaGory, K., McDonald,  
952 K., and Steiner, N.: An integrated assessment approach for estimating the  
953 economic impacts of climate change on River systems: An application to  
954 hydropower and fisheries in a Himalayan River, Trishuli, *Environmental Science  
955 & Policy*, 87, 102-111, 10.1016/j.envsci.2018.05.006, 2018.

956 Mishra, S. K., Rupper, S., Kapnick, S., Casey, K., Chan, H. G., Ciraci, E., Haritashya,  
957 U., Hayse, J., Kargel, J. S., Kayastha, R. B., Krakauer, N. Y., Kumar, S. V.,  
958 Lammers, R. B., Maggioni, V., Margulis, S. A., Olson, M., Osmanoglu, B., Qian,  
959 Y., McLarty, S., Rittger, K., Rounce, D. R., Shean, D., Velicogna, I., Veselka, T.  
960 D., and Arendt, A.: Grand challenges of hydrologic modeling for food-energy-  
961 water nexus security in High Mountain Asia, *Frontiers in Water*, 3,

962 10.3389/frwa.2021.728156, 2021.

963 Negi, H. S. and Kokhanovsky, A.: Retrieval of snow grain size and albedo of western  
964 Himalayan snow cover using satellite data, *The Cryosphere*, 5, 831-847,  
965 10.5194/tc-5-831-2011, 2011.

966 Notarnicola, C.: Hotspots of snow cover changes in global mountain regions over  
967 2000–2018, *Remote Sensing of Environment.*, 243, 111781,  
968 10.1016/j.rse.2020.111781, 2020.

969 Niu, X., Pu, W., Fu, P., Chen, Y., Xing, Y., Wu, D., Chen, Z., Shi, T., Zhou, Y., Wen, H.,  
970 and Wang, X.: Fluorescence characteristics, absorption properties, and radiative  
971 effects of water-soluble organic carbon in seasonal snow across northeastern China,  
972 *Atmospheric Chemistry and Physics*, 22, 14075-14094, 10.5194/acp-22-14075-  
973 2022, 2022.

974 Okada, K., Kai, K.: Atmospheric mineral particles collected at Qira in the Taklamakan  
975 Desert, China, *Atmospheric Environment*, 38, 6927-6935,  
976 10.1016/j.atmosenv.2004.03.078, 2004.

977 Orsolini, Y., Wegmann, M., Dutra, E., Liu, B., Balsamo, G., Yang, K., de Rosnay, P.,  
978 Zhu, C., Wang, W., Senan, R., and Arduini, G.: Evaluation of snow depth and snow  
979 cover over the Tibetan Plateau in global reanalyses using in situ and satellite  
980 remote sensing observations, *The Cryosphere*, 13, 2221-2239, 10.5194/tc-13-  
981 2221-2019, 2019.

982 Painter, T. H., Rittger, K., McKenzie, C., Slaughter, P., Davis, R. E., and Dozier, J.:  
983 Retrieval of subpixel snow covered area, grain size, and albedo from MODIS,  
984 *Remote Sensing of Environment*, 113, 868-879, 10.1016/j.rse.2009.01.001, 2009.

985 Painter, T. H., Bryant, A. C., and Skiles, S. M.: Radiative forcing by light absorbing  
986 impurities in snow from MODIS surface reflectance data, *Geophysical Research*  
987 *Letters*, 39, n/a-n/a, 10.1029/2012gl052457, 2012.

988 Painter, T. H., Skiles, S. M., Deems, J. S., Brandt, W. T., and Dozier, J.: Variation in  
989 rising limb of colorado river snowmelt runoff hydrograph controlled by dust  
990 radiative forcing in snow, *Geophysical Research Letters*, 45, 797-808,  
991 10.1002/2017gl075826, 2017.

992 Patterson, E.M.: Optical properties of the crustal aerosol: Relation to chemical and  
993 physical characteristics, *Journal of Geophysical Research: Atmospheres*, 86, 3236-  
994 3246, 10.1029/JC086iC04p03236, 1981.

995 Pu, W., Cui, J., Shi, T., Zhang, X., He, C., and Wang, X.: The remote sensing of radiative  
996 forcing by light-absorbing particles (LAPs) in seasonal snow over northeastern  
997 China, *Atmospheric Chemistry and Physics*, 19, 9949-9968, 10.5194/acp-19-  
998 9949-2019, 2019.

999 Pu, W., Cui, J., Wu, D., Shi, T., Chen, Y., Xing, Y., Zhou, Y., and Wang, X.:  
1000 Unprecedented snow darkening and melting in New Zealand due to 2019–2020  
1001 Australian wildfires, *Fundamental Research*, 1, 224-231,  
1002 10.1016/j.fmre.2021.04.001, 2021.

1003 Pulliainen, J., Luojus, K., Derksen, C., Mudryk, L., Lemmetyinen, J., Salminen, M.,  
1004 Ikonen, J., Takala, M., Cohen, J., Smolander, T., and Norberg, J.: Patterns and  
1005 trends of Northern Hemisphere snow mass from 1980 to 2018, 581, 294-298,

1006 s41586-020-2258-0, 2020.

1007 Qian, Y., Yasunari, T. J., Doherty, S. J., Flanner, M. G., Lau, W. K. M., Ming, J., Wang,  
1008 H., Wang, M., Warren, S. G., and Zhang, R.: Light-absorbing particles in snow and  
1009 ice: Measurement and modeling of climatic and hydrological impact, *Advances in*  
1010 *Atmospheric Sciences*, 32, 64-91, 10.1007/s00376-014-0010-0, 2015.

1011 Qiu, X., Zeng, Y., and Miao, Q.: Sand-dust storms in China: temporal-spatial  
1012 distribution and tracks of source lands, *Journal of Geographical Sciences*. 11, 253–  
1013 260, 10.1007/BF02892308, 2001.

1014 Reveillet, M., Dumont, M., Gascoïn, S., Lafaysse, M., Nabat, P., Ribes, A., Nheili, R.,  
1015 Tuzet, F., Menegoz, M., Morin, S., Picard, G., and Ginoux, P.: Black carbon and  
1016 dust alter the response of mountain snow cover under climate change, *Nature*  
1017 *Communication*, 13, 5279, 10.1038/s41467-022-32501-y, 2022.

1018 Ricchiazzi, P., Yang, S. R., Gautier, C., and Sowle, D.: SBDART: A research and  
1019 teaching software tool for plane-parallel radiative transfer in the Earth's  
1020 atmosphere, *Bulletin of the American Meteorological Society.*, 79, 2101–2114,  
1021 10.1175/1520-0477(1998)079<2101:Sarats>2.0.Co;2, 1998.

1022 Rittger, K., Painter, T. H., and Dozier, J.: Assessment of methods for mapping snow  
1023 cover from MODIS, *Advances in Water Resources*, 51, 367-380,  
1024 10.1016/j.advwatres.2012.03.002, 2013.

1025 Rohde, A., Vogel, H., Hoshyaripour, H. A., Kottmeier C., and Vogel, B.: Regional  
1026 Impact of Snow-Darkening on Snow Pack and the Atmosphere During a Severe  
1027 Saharan Dust Deposition Event in Eurasia, *Journal of Geophysical Research:*  
1028 *Earth Surface*, 128, 10.1029/2022JF007016, 2023.

1029 Roychoudhury, C., He, C., Kumar, R., McKinnon, J. M., and Arellano, A. F.: On the  
1030 relevance of aerosols to snow cover variability over High Mountain Asia,  
1031 *Geophysical Research Letters*, 49, 10.1029/2022gl099317, 2022.

1032 Sang, J., Kim, M.-K., Lau, W. K. M., and Kim, K.-M.: Possible Impacts of snow  
1033 darkening effects on the hydrological cycle over western Eurasia and east Asia,  
1034 *Atmosphere*, 10, 10.3390/atmos10090500, 2019.

1035 Sarangi, C., Qian, Y., Rittger, K., Bormann, K. J., Liu, Y., Wang, H., Wan, H., Lin, G.,  
1036 and Painter, T. H.: Impact of light-absorbing particles on snow albedo darkening  
1037 and associated radiative forcing over high-mountain Asia: high-resolution WRF-  
1038 Chem modeling and new satellite observations, *Atmospheric Chemistry and*  
1039 *Physics*, 19, 7105-7128, 10.5194/acp-19-7105-2019, 2019.

1040 Sarangi, C., Qian, Y., Rittger, K., Ruby Leung, L., Chand, D., Bormann, K. J., and  
1041 Painter, T. H.: Dust dominates high-altitude snow darkening and melt over high-  
1042 mountain Asia, *Nature Climate Change*, 10, 1045-1051, 10.1038/s41558-020-  
1043 00909-3, 2020.

1044 Schmale, J., Flanner, M., Kang, S. C., Sprenger, M., Zhang, Q. G., Guo, J. M., Li, Y.,  
1045 Schwikowski, M., and Farinotti, D.: Modulation of snow reflectance and  
1046 snowmelt from Central Asian glaciers by anthropogenic black carbon, *Scientific*  
1047 *Reports*, 7, 40501, 10.1038/srep40501, 2017.

1048 Siegmund., A. and Menz., G.: Fernes nah gebracht – satelliten- und luftbildeinsatz zur  
1049 analyse von umweltveränderungen im geographieunterricht, *Geographie und*



1050 Schule, 154, 2–10, 2005.

1051 Shao, Y. and Dong, C. H.: A review on East Asian dust storm climate, modelling and  
1052 monitoring, *Global and Planetary Change*, 52, 1–22,  
1053 10.1016/j.gloplacha.2006.02.011, 2006.

1054 She, J., Zhang, Y., Li, X., and Feng, X.: Spatial and temporal characteristics of snow  
1055 cover in the Tizinafu watershed of the Western Kunlun Mountains, *Remote  
1056 Sensing*, 7, 3426–3445, 10.3390/rs70403426, 2015.

1057 Shi, T., Pu, W., Zhou, Y., Cui, J., Zhang, D., and Wang, X.: Albedo of black carbon-  
1058 contaminated snow across Northwestern China and the validation with model  
1059 simulation, *Journal of Geophysical Research: Atmospheres*, 125,  
1060 10.1029/2019jd032065, 2020.

1061 Shi, T., Cui, J., Chen, Y., Zhou, Y., Pu, W., Xu, X., Chen, Q., Zhang, X., and Wang, X.:  
1062 Enhanced light absorption and reduced snow albedo due to internally mixed  
1063 mineral dust in grains of snow, *Atmospheric Chemistry and Physics*, 21, 6035–  
1064 6051, 10.5194/acp-21-6035-2021, 2021.

1065 Shi, T., Cui, J., Wu, D., Xing, Y., Chen, Y., Zhou, Y., Pu, W., and Wang, X.: Snow albedo  
1066 reductions induced by the internal/external mixing of black carbon and mineral  
1067 dust, and different snow grain shapes across northern China, *Environmental  
1068 Research*, 208, 112670, 10.1016/j.envres.2021.112670, 2022a.

1069 Shi, T., Chen, Y., Xing, Y., Niu, X., Wu, D., Cui, J., Zhou, Y., Pu, W., and Wang, X.:  
1070 Assessment of the combined radiative effects of black carbon in the atmosphere  
1071 and snowpack in the Northern Hemisphere constrained by surface observations,  
1072 *Environmental Science: Atmospheres*, 2, 702–713, 10.1039/d2ea00005a, 2022b.

1073 Shi, Z., Xie, X., Li, X., Yang, L., Xie, X., Lei, J., Sha, Y., and Liu, X.: Snow-darkening  
1074 versus direct radiative effects of mineral dust aerosol on the Indian summer  
1075 monsoon onset: role of temperature change over dust sources, *Atmospheric  
1076 Chemistry and Physics*, 19, 1605–1622, 10.5194/acp-19-1605-2019, 2019.

1077 Skiles, S. M. and Painter, T.: Daily evolution in dust and black carbon content, snow  
1078 grain size, and snow albedo during snowmelt, Rocky Mountains, Colorado,  
1079 *Journal of Glaciology*, 63, 118–132, 10.1017/jog.2016.125, 2016.

1080 Skiles, S. M., Flanner, M., Cook, J. M., Dumont, M., and Painter, T. H.: Radiative  
1081 forcing by light-absorbing particles in snow, *Nature Climate Change*, 8, 964–971,  
1082 10.1038/s41558-018-0296-5, 2018a.

1083 Skiles, S. M., Mallia, D. V., Hallar, A. G., Lin, J. C., Lambert, A., Petersen, R., and  
1084 Clark, S.: Implications of a shrinking Great Salt Lake for dust on snow deposition  
1085 in the Wasatch Mountains, UT, as informed by a source to sink case study from  
1086 the 13–14 April 2017 dust event, *Environmental Research Letters*, 13,  
1087 10.1088/1748-9326/aaefd8, 2018b.

1088 Sun, J., Zhang, M., and Liu, T.: Spatial and temporal characteristics of dust storms in  
1089 China and its surrounding regions, 1960–1999: Relations to source area and  
1090 climate, *Journal of Geophysical Research: Atmospheres*, 106, 10325–10333,  
1091 10.1029/2000jd900665, 2001.

1092 Tang, W., Dai, T., Cheng, Y., Wang, S., and Liu, Y.: A study of a severe spring dust event  
1093 in 2021 over east Asia with WRF-Chem and multiple platforms of observations,

1094 Remote Sensing, 14, 10.3390/rs14153795, 2022.

1095 Teillet, P. M., Guindon, B., and Goodenough, D. G.: On the slope-aspect correction of  
1096 multispectral scanner data, *Canadian Journal of Remote Sensing*, 8, 84-106,  
1097 10.1080/07038992.1982.10855028, 1982.

1098 Thakur, R. C., Arun, B. S., Gogoi, M. M., Thamban, M., Thayyen, R. J., Redkar, B. L.,  
1099 and Suresh Babu, S.: Multi-layer distribution of Black Carbon and inorganic ions  
1100 in the snowpacks of western Himalayas and snow albedo forcing, *Atmospheric  
1101 Environment*, 261, 10.1016/j.atmosenv.2021.118564, 2021.

1102 Usha, K. H., Nair, V. S., and Babu, S. S.: Deciphering the role of aerosol-induced snow  
1103 albedo feedback on dust emission over the Tibetan Plateau, *Journal of Geophysical  
1104 Research: Atmospheres*, 127, 10.1029/2021jd036384, 2022.

1105 Wake, C. P., Mayewski, P. A., Li, Z., Han, J., and Qin, D.: Modern eolian dust deposition  
1106 in central Asia, *Tellus B: Chemical and Physical Meteorology*, 46,  
1107 10.3402/tellusb.v46i3.15793, 1994.

1108 Wang, X., Huang, J., Ji, M., and Higuchi, K.: Variability of East Asia dust events and  
1109 their long-term trend, *Atmospheric Environment*, 42, 3156-3165,  
1110 10.1016/j.atmosenv.2007.07.046, 2008.

1111 Wang, X., Doherty, S. J., and Huang, J.: Black carbon and other light-absorbing  
1112 impurities in snow across Northern China, *Journal of Geophysical Research:  
1113 Atmospheres*, 118, 1471-1492, 10.1029/2012jd018291, 2013.

1114 Wang, X., Pu, W., Ren, Y., Zhang, X., Zhang, X., Shi, J., Jin, H., Dai, M., and Chen, Q.:  
1115 Observations and model simulations of snow albedo reduction in seasonal snow  
1116 due to insoluble light-absorbing particles during 2014 Chinese survey,  
1117 *Atmospheric Chemistry and Physics*, 17, 2279-2296, 10.5194/acp-17-2279-2017,  
1118 2017.

1119 Wang, X., Wei, H., Liu, J., Xu, B., Wang, M., Ji, M., and Jin, H.: Quantifying the light  
1120 absorption and source attribution of insoluble light-absorbing particles on Tibetan  
1121 Plateau glaciers between 2013 and 2015, *The Cryosphere*, 13, 309-324,  
1122 10.5194/tc-13-309-2019, 2019.

1123 Wei, T., Dong, Z., Kang, S., Qin, X., and Guo, Z.: Geochemical evidence for sources  
1124 of surface dust deposited on the Laohugou glacier, Qilian Mountains, *Applied  
1125 Geochemistry*, 79, 1-8, 10.1016/j.apgeochem.2017.01.024, 2017.

1126 Wiscombe, W. J. and Warren, S. G.: A model for the spectral albedo of snow .1. Pure  
1127 snow, *Journal of the Atmospheric Sciences*, 37, 2712-2733,  
1128 10.1175/15200469(1980)037<2712:Amftsa>2.0.Co;2, 1980.

1129 Wu, D., Liu, J., Wang, T., Niu, X., Chen, Z., Wang, D., Zhang, X., Ji, M., Wang, X.,  
1130 and Pu, W.: Applying a dust index over North China and evaluating the  
1131 contribution of potential factors to its distribution, *Atmospheric Research*, 254,  
1132 10.1016/j.atmosres.2021.105515, 2021.

1133 Wu, G., Yao, T., Xu, B., Tian, L., Zhang, C., and Zhang, X.: Dust concentration and  
1134 flux in ice cores from the Tibetan Plateau over the past few decades, *Tellus B:  
1135 Chemical and Physical Meteorology*, 62, 10.1111/j.1600-0889.2010.00457.x,  
1136 2010.

1137 Xu, J., Kang, S., Hou, S., Zhang, Q., Huang, J., Xiao, C., Ren, J., and Qin, D.:

1138 Characterization of contemporary aeolian dust deposition on mountain glaciers of  
1139 western China, *Sci. Cold Arid Reg*, 8, 0009-0021, 2016.

1140 Yang, L., Shi, Z., Xie, X., Li, X., Liu, X., and An, Z.: Seasonal changes in East Asian  
1141 monsoon-westerly circulation modulated by the snow-darkening effect of mineral  
1142 dust, *Atmospheric Research*, 279, 10.1016/j.atmosres.2022.106383, 2022.

1143 Yao, T., Thompson, L., Yang, W., Yu, W., Gao, Y., Guo, X., Yang, X., Duan, K., Zhao,  
1144 H., Xu, B., Pu, J., Lu, A., Xiang, Y., Kattel, D. B., and Joswiak, D.: Different  
1145 glacier status with atmospheric circulations in Tibetan Plateau and surroundings,  
1146 *Nature Climate Change*, 2, 663-667, 10.1038/nclimate1580, 2012.

1147 Yao, T., Xue, Y., Chen, D., Chen, F., Thompson, L., Cui, P., Koike, T., Lau, W. K. M.,  
1148 Lettenmaier, D., Mosbrugger, V., Zhang, R., Xu, B., Dozier, J., Gillespie, T., Gu,  
1149 Y., Kang, S., Piao, S., Sugimoto, S., Ueno, K., Wang, L., Wang, W., Zhang, F.,  
1150 Sheng, Y., Guo, W., Ailikun, Yang, X., Ma, Y., Shen, S. S. P., Su, Z., Chen, F.,  
1151 Liang, S., Liu, Y., Singh, V. P., Yang, K., Yang, D., Zhao, X., Qian, Y., Zhang, Y.,  
1152 and Li, Q.: Recent Third Pole's rapid warming accompanies cryospheric melt and  
1153 water cycle intensification and interactions between monsoon and environment:  
1154 Multidisciplinary approach with observations, modeling, and analysis, *Bulletin of  
1155 the American Meteorological Society*, 100, 423-444, 10.1175/bams-d-17-0057.1,  
1156 2019.

1157 Yuan, T., Chen, S., Huang, J., Wu, D., Lu, H., Zhang, G., Ma, X., Chen, Z., Luo, Y., and  
1158 Ma, X.: Influence of dynamic and thermal forcing on the meridional transport of  
1159 Taklimakan desert dust in spring and summer, *Journal of Climate*, 32, 749-767,  
1160 10.1175/jcli-d-18-0361.1, 2018.

1161 Zege, E. P., Katsev, I. L., Malinka, A. V., Prikhach, A. S., Heygster, G., and Wiebe, H.:  
1162 Algorithm for retrieval of the effective snow grain size and pollution amount from  
1163 satellite measurements, *Remote Sensing of Environment*, 115, 2674-2685,  
1164 10.1016/j.rse.2011.06.001, 2011.

1165 Zhang, B., Tsunekawa, A., and Tsubo, M.: Contributions of sandy lands and stony  
1166 deserts to long-distance dust emission in China and Mongolia during 2000–2006,  
1167 *Global and Planetary Change*, 60, 487-504, 10.1016/j.gloplacha.2007.06.001,  
1168 2008.

1169 Zhang, X., Li, Z. Q., You, X. N., She, Y. Y., Song, M. Y., and Zhou, X.: Light-Absorbing  
1170 Impurities on Urumqi Glacier No.1 in Eastern Tien Shan: Concentrations and  
1171 Implications for Radiative Forcing Estimates During the Ablation Period,  
1172 *Frontiers in Earth Science*, 9, 2296-6463, 10.3389/feart.2021.524963, 2021.

1173 Zhang, Y., Kang, S., Sprenger, M., Cong, Z., Gao, T., Li, C., Tao, S., Li, X., Zhong, X.,  
1174 Xu, M., Meng, W., Neupane, B., Qin, X., and Sillanpää, M.: Black carbon and  
1175 mineral dust in snow cover on the Tibetan Plateau, *The Cryosphere*, 12, 413-431,  
1176 10.5194/tc-12-413-2018, 2018.

1177 Zhang, Y., Gao, T., Kang, S., Sprenger, M., Tao, S., Du, W., Yang, J., Wang, F., and  
1178 Meng, W.: Effects of black carbon and mineral dust on glacial melting on the Muz  
1179 Taw glacier, Central Asia, *Science of the Total Environment*, 740, 140056,  
1180 10.1016/j.scitotenv.2020.140056, 2020.

1181 Zhang, Y., Gao, T., Kang, S., Shangguan, D., and Luo, X.: Albedo reduction as an

1182 important driver for glacier melting in Tibetan Plateau and its surrounding areas,  
1183 Earth-Science Reviews, 220, 10.1016/j.earscirev.2021.103735, 2021.

1184 Zhao, X., Huang, K., Fu, J. S., and Abdullaev, S. F.: Long-range transport of Asian dust  
1185 to the Arctic: identification of transport pathways, evolution of aerosol optical  
1186 properties, and impact assessment on surface albedo changes, Atmospheric  
1187 Chemistry and Physics, 22, 10389-10407, 10.5194/acp-22-10389-2022, 2022.

1188 Zhu, L., Ma, G., Zhang, Y., Wang, J., Tian, W., and Kan, X.: Accelerated decline of  
1189 snow cover in China from 1979 to 2018 observed from space, Science of the Total  
1190 Environment, 814, 152491, 10.1016/j.scitotenv.2021.152491, 2022.

1191  
1192  
1193